
Research Article: New Research | Disorders of the Nervous System

Time course of alterations in adult spinal motoneuron properties in the SOD1(G93A) mouse model of ALS

<https://doi.org/10.1523/ENEURO.0378-20.2021>

Cite as: eNeuro 2021; 10.1523/ENEURO.0378-20.2021

Received: 30 August 2020

Revised: 25 January 2021

Accepted: 26 January 2021

This Early Release article has been peer-reviewed and accepted, but has not been through the composition and copyediting processes. The final version may differ slightly in style or formatting and will contain links to any extended data.

Alerts: Sign up at www.eneuro.org/alerts to receive customized email alerts when the fully formatted version of this article is published.

Copyright © 2021 Huh et al.

This is an open-access article distributed under the terms of the Creative Commons Attribution 4.0 International license, which permits unrestricted use, distribution and reproduction in any medium provided that the original work is properly attributed.

1 **Time course of alterations in adult spinal motoneuron**
2 **properties in the SOD1(G93A) mouse model of ALS**

3 **Seoan Huh¹, Charles J. Heckman^{1,2,3}, and Marin Manuel^{1,4,§}**

4 ¹Department of Physiology, ²Department of Physical Medicine and Rehabilitation,
5 and ³Department of Physical Therapy and Human Movement Science, Northwestern
6 University, Feinberg School of Medicine, Chicago, Illinois, USA. ⁴Université de Paris,
7 SPPIN - Saints-Pères Paris Institute for the Neurosciences, CNRS, Paris, France.

8

9 **§ Corresponding author:**

10 Marin MANUEL
11 SPPIN - Saints-Pères Paris Institute for the Neurosciences
12 Université de Paris, 45, rue des Saints-Pères, 75006 Paris, France
13 email: marin.manuel@neurobio.org

14

15 **Author contribution**

16 Conceptualization: S.H., C.J.H., and M.M.; Methodology: S.H., C.J.H., and M.M.;
17 Investigation: S.H.; Formal analysis: S.H. and M.M.; Software: M.M.; Visualization: S.H.
18 and M.M.; Writing - Original Draft: S.H.; Writing - Review & Editing: S.H., C.J.H., and
19 M.M.; Funding Acquisition: C.J.H and M.M.; S.H., C.J.H., and M.M. approved the final
20 version of this manuscript.

21

22 **Conflict of Interest**

23 The authors have no conflict of interest to declare

24 **Acknowledgments**

25 This work was supported by NIH NINDS R01NS077863 and NINDS R01NS110953.
26 S.H. was supported by a National Science Foundation Graduate Research Fellowship
27 (NSF GRFP).

28 **Abstract**

29 Although ALS is an adult-onset neurodegenerative disease, motoneuron electrical
30 properties are already altered during embryonic development. Motoneurons must
31 therefore exhibit a remarkable capacity for homeostatic regulation to maintain a
32 normal motor output for most of the life of the patient. In the present paper, we
33 demonstrate how maintaining homeostasis could come at a very high cost. We
34 studied the excitability of spinal motoneurons from young adult SOD1(G93A) mice
35 to end-stage. Initially homeostasis is highly successful in maintaining their overall
36 excitability. This initial success, however, is achieved by pushing some cells far
37 above the normal range of passive and active conductances. As the disease
38 progresses, both passive and active conductances shrink below normal values in the
39 surviving cells. This shrinkage may thus promote survival, implying the previously
40 large values contribute to degeneration. These results support the hypothesis that
41 motoneuronal homeostasis may be “hyper-vigilant” in ALS and a source of
42 accumulating stress.

43 **Significance Statement**

44 During ALS, motoneurons exhibit a remarkable ability to maintain a normal
45 motor output despite continuous alterations of their electrophysiological properties,
46 up to the point when overt symptoms become apparent. We show that this
47 homeostatic process can sometimes push motoneurons beyond the normal range,
48 which may be causing long-lasting harm.

49 **Introduction**

50 ALS is a fatal neurodegenerative disorder characterized by progressive loss of
51 cortical and spinal motoneurons. Five to ten percent of the ALS cases are familial
52 (FALS), and ~20% of the FALS cases are due to mutations in the Superoxide
53 Dismutase1 (SOD1) gene (Rosen et al., 1993). Studies in the mutant SOD1 (mSOD1)
54 mouse and other animal models have revealed that multiple cellular functions
55 become impaired as the disease progresses (Ilieva et al., 2009; Kanning et al., 2009;
56 Johnson and Heckman, 2010; Brownstone and Lancelin, 2018), implying that
57 homeostatic mechanisms are failing. Yet, the intrinsic excitability of neonatal and
58 young adult mSOD1 motoneurons undergoes a very potent and effective
59 homeostatic response to compensate for an earlier surge in excitability in the
60 embryonic state (Kuo et al., 2004; van Zundert et al., 2008; Pieri et al., 2009; Martin
61 et al., 2013). The mechanisms of this successful homeostasis are however highly
62 unusual.

63 The standard measure of the net excitability of motoneurons is the relation
64 between the frequency of firing and the amplitude of the injected current. Multiple
65 ionic currents contribute to this frequency-current (F-I) function relationship. Chief
66 among them are persistent inward currents (PICs), which are mediated by voltage-
67 gated Na⁺ and Ca²⁺ channels. In neonatal mSOD1 mice, PICs in spinal motoneurons
68 become aberrantly large (Quinlan et al., 2011). On its own, this change would
69 increase F-I gain, but it is compensated by commensurate increases in the leak
70 currents that set the input conductance of the cell, so that the net excitability
71 remains constant (Quinlan et al., 2011). These abnormal changes show that F-I

72 homeostasis during the neonatal period is achieved via a compensatory mechanism.
73 If, however, these compensatory increases persist into the young adult state, then
74 the continued distortions in input conductances and PIC amplitudes could induce a
75 substantial stress within the motoneurons. Increasing the number of leak
76 conductances and voltage-gated channels implies a higher energy expenditure to
77 maintain the resting membrane potential and ionic gradients across the membrane,
78 which already occupies a large share of the metabolic budget of neurons (Attwell
79 and Laughlin, 2001; Herculano-Houzel, 2011; Howarth et al., 2012). One must also
80 consider the additional burden associated with the increased housekeeping tasks
81 such as lipid synthesis, trafficking of organelles and protein synthesis, which
82 account for 25–50% of the energy budget of neurons (Rolfe and Brown, 1997;
83 Attwell and Laughlin, 2001). In this scenario, the initial success in the homeostatic
84 regulation of net excitability would come at a severe cost, likely accelerating the
85 onset of degeneration. Indeed, neurons function on a very restricted energy budget
86 that is independent of their size (Herculano-Houzel, 2011). On the other hand, if
87 homeostatic processes instead successfully return input conductance and PIC values
88 to normal ranges before the onset of denervation, then homeostasis for the F-I
89 function would reduce stress on the cell and effects on subsequent degeneration
90 would likely be small.

91 To investigate how homeostasis for excitability develops as the disease
92 progresses, we undertook the first *in vivo* voltage-clamp studies of motoneurons in
93 the SOD1(G93A) mouse model of ALS and pursued these measurements across a
94 wide range of ages, from P30 to P120. This age range spans the young adult period,

95 the onset of denervation period (~P50, Pun et al., 2006), and the development of
96 overt symptoms (~P90). Because adult mSOD1 motoneurons tend to have a larger
97 input conductance than controls (Delestrée et al., 2014), we hypothesized that input
98 conductance and PIC values would continue to grow in the young adult state. Our
99 results supported this hypothesis, revealing, in fact, a continual increase in the
100 amplitude of these parameters, followed by a collapse, so that motoneurons
101 surviving beyond the onset of overt symptoms (~P90) had aberrantly small values
102 of each. These results are consistent with the possibility that homeostasis for
103 excitability is not weak but excessively strong and that this overreaction contributes
104 to subsequent degeneration (Mitchell and Lee, 2012).

105 **Methods**

106 **Animals**

107 This study was performed in strict accordance with the recommendations in the
108 Guide for the Care and Use of Laboratory Animals of the National Institutes of
109 Health. All of the animals were handled according to protocols approved by
110 Northwestern University's institutional animal care and use committee (IACUC). All
111 surgery was performed under sodium pentobarbital anesthesia, and every effort
112 was made to minimize suffering. Because of the reproducible and stereotyped
113 progression of symptoms, we chose to use mice overexpressing the human
114 SOD1(G93A) gene, in which glycine has been substituted by alanine at residue 93 as
115 a mouse model of ALS. Hemizygous transgenic mutant males were bred with B6SJL
116 F1 females (obtained from the Jackson Laboratory, Bar Harbor, ME)(Leitner et al.,

117 2009). Offspring were genotyped and the transgene copy number was compared to
118 a housekeeping gene at Transnetyx (Cordova, TN). Only mice with relative copy
119 number >45 were used in this study. The control group consisted of non-transgenic
120 littermates, with the same B6SJL background (WT). 33 animals of either sex were
121 used in this study. Because these experiments tend to have a higher success rate
122 with larger animals, our sample was biased towards males (27 males and 6
123 females). Animals were divided into different age groups for analysis: animals
124 whose age was <60 days-old were categorized as P30–60 (N=9 mice), animals
125 whose age was ≥60 and <90 as P60–90 (N=12 mice), and animals older than
126 ≥90 days-old were classified as P90–120 (N=12 mice).

127 **In vivo preparation**

128 Procedures were similar to those in our previous studies (Manuel and Heckman,
129 2011). Initially, atropine (0.2 mg/kg) was administered subcutaneously to prevent
130 salivation. Ten minutes later, anesthesia was initiated with an intraperitoneal
131 injection of pentobarbital sodium (70 mg/kg) and maintained by intravenous
132 infusion of supplemental doses of pentobarbital (6 mg/kg) mixed in perfusion
133 solution containing 4% glucose, 1% NaHCO₃, and 14% Plasmion. The trachea was
134 cannulated, allowing the mouse to be artificially ventilated with 100% O₂. The end-
135 tidal PCO₂ was continuously monitored and maintained around 4% by adjusting
136 ventilator parameters including respiratory rate around 120–150 bpm and tidal
137 volume around 0.09–0.23 mL. The hind limb muscles were then dissected; biceps
138 femoris was removed to expose the sciatic nerve, which was thereafter placed over
139 a stimulating electrode. A laminectomy was performed at the T13–L1 level and the

140 L3–L4 spinal segments were exposed. To prevent the spinal cord from dehydration,
141 a custom made bath was affixed using silicone elastomer and covered with mineral
142 oil. To locate the motoneurons of interest, the sciatic nerve was stimulated at 1.8–2×
143 the minimum intensity required to observe an afferent volley.

144 **Electrophysiology**

145 Intracellular recordings of spinal motoneurons were performed by impaling them
146 with glass micropipette electrodes filled with 3M KCl with a resistance of 8–15 MΩ.
147 Motoneurons were identified by the presence of antidromic action potential from
148 stimulation of the sciatic nerve. Cells with unstable resting membrane potential
149 (RMP) or with RMP more depolarized than –50 mV were excluded from the analysis.
150 We record a median of 3 cells per animal (average ± SD 3.1±1.7 cells per animal,
151 mode 2 cells/animal, N=33).

152 PICs were recorded in discontinuous voltage-clamp mode, with switching rates of
153 6–8 kHz. Clamp feedback gain was between 0.3 and 1.5. In addition to the feedback
154 gain from the Axoclamp amplifier, an additional low-frequency feedback loop with a
155 gain of 11 and a cutoff of –3 dB at 0.3 kHz was used to improve voltage control in
156 such large cells as motoneurons (Lee and Heckman, 1998). Monitoring outputs were
157 observed at all times to assure reasonable settling of the electrode. To record PICs, a
158 slow triangular voltage ramp (–80 to –40 mV) was applied (Lee and Heckman,
159 1998). Leak current was determined by fitting a regression line through the
160 subthreshold region (–80 to –65 mV) of the I-V function. Then, this leak was
161 subtracted from the total function to determine the PIC amplitude (measured both
162 on the ascending and descending part of the ramp). In addition, the voltage at which

163 the PIC was maximal on each part of the ramp was recorded (PIC peak voltage). The
164 PIC onset voltage was estimated on the leak-subtracted trace as the point where the
165 curve started to visibly deviate downward from the horizontal. Input conductance
166 was estimated as the slope of the leak current.

167 To assess the intrinsic properties of the motoneuron in current-clamp mode, we
168 measured the frequency-current (F-I) relationship of action potential firing. The F-I
169 relationship was determined based on the firing produced by a triangular current
170 injection. The interspike frequency was then plotted against the intensity of the
171 injected current. All these measurements were carried out in the discontinuous
172 current-clamp mode of the Axoclamp 2A amplifier, with switching rates of 6–8 kHz.
173 Mouse motoneurons possess two regimes of firing: a sub-primary range of firing,
174 followed by a linear primary range (Manuel et al., 2009; Manuel and Heckman,
175 2011). The primary range was identified visually starting from the top of the ramp
176 and going backward towards the beginning (for the ascending ramp) of forward
177 towards the end (for the descending ramp). A linear portion of the instantaneous
178 frequency, with low variability, can generally be easily identified before a sudden
179 change of slope or an increase in firing variability. The “gain” of the F-I relationship
180 was determined by fitting a regression line over the linear range so identified
181 (separately on the ascending and descending phase of the ramp). The other
182 parameters measured in the F-I relationship were: the current at which the first
183 action potential (AP) fires on the ascending ramp (recruitment current), the current
184 at which the last AP fires on the descending ramp (current at de-recruitment); the
185 voltage threshold for spiking, which was determined as the voltage where the slope

186 of the membrane voltage reaches 10 mV/ms before the first AP (Sekerli et al., 2004);
187 the current and firing frequency at the transition between the sub-primary and
188 primary ranges (Manuel and Heckman, 2011).

189 **Data analysis**

190 Recordings were acquired and analyzed using Spike2 v.7 (CED, Cambridge, UK).
191 Data were analyzed using the scientific python (v.3.7.4) ecosystem: Pandas v.1.0.5
192 (McKinney, 2011), SciPy v.1.5.2 (Virtanen et al., 2020), DABEST v.0.3.0 (Ho et al.,
193 2019), statsmodels v.0.12.0 (Seabold and Perktold, 2010) and scikit-learn v.0.23.0
194 (Pedregosa et al., 2011). Figures were generated using matplotlib v.3.1.3 (Hunter,
195 2007) and seaborn v.0.10.0 (Waskom et al., 2020).

196 **Statistical analysis**

197 All data are reported as mean \pm standard deviation with their respective sample
198 size. Each cell is treated as an independent observation, and the reported N refers to
199 the number of cells, unless otherwise specified. No test was performed to detect
200 outliers, and no data points were excluded from the analysis. When comparing
201 between WT and mSOD1 samples, we focus on estimation statistics that rely on
202 effect sizes and confidence intervals (95%CI), rather than null hypothesis
203 significance testing, as recommended by several scientific societies and editorial
204 boards (Bernard, 2019; Makin and Orban de Xivry, 2019; Wasserstein et al., 2019;
205 Michel et al., 2020). Unless otherwise specified, effect sizes are reported as
206 differences of means and Hedges' g (Hedges, 2016). Where appropriate, data are
207 presented as Cumming plots (Cumming, 2012) generated using DABEST. In these
208 plots, the raw data are plotted as swarms of points. In addition, the mean \pm standard

209 deviation of each group is plotted as a notched line immediately to the right of each
210 group. The effect size and bootstrapped 95% CIs are plotted on separate axes
211 beneath the raw data. Confidence intervals were bias-corrected and accelerated, and
212 are displayed with the bootstrap distribution of the mean; resampling was
213 performed 5000 times (Ho et al., 2019). Welch's *t*-test (Welch, 1947) results are
214 provided for information only. ANCOVA was performed using statsmodels' OLS
215 routines, fitting the model "PIC amplitude ~ input conductance * Genotype". No
216 significant interaction term was detected for any of the age groups considered, and
217 the model was run again without interaction. Dimensionality reduction was
218 performed using scikit-learn's PCA. The 21 electrophysiological features (which did
219 not include genotype or age) of our dataset were centered and scaled then projected
220 on a 5D space. For analysis, only the first three principal components were
221 considered.

222 **Results**

223 We set out to compare neuronal excitability, in 103 motoneurons from
224 SOD1(G93A) mice (mSOD1), and their non-transgenic (WT) littermate, aged
225 between 31 and 123 days old. Neuronal excitability was estimated on the response
226 of the motoneurons to a triangular ramp of current in current-clamp mode. In
227 addition, PICs were measured in each motoneuron using a triangular voltage ramp
228 in voltage-clamp mode. Most of the values measured on the ascending and
229 descending phases of the ramps, both in voltage-clamp and current-clamp were very
230 strongly correlated (PIC amplitude on ascending and descending ramps: $r^2=0.75$;

231 PIC onset voltage: $r^2=0.89$; PIC peak voltage: $r^2=0.90$; recruitment and de-
232 recruitment currents: $r^2=0.90$). For this reason, we will mostly focus on the
233 parameters measured on the ascending ramp.

234 Given the large period considered here, one also needs to consider whether
235 alterations in motoneuron properties were direct effects of the mutation or merely
236 shifts in the distribution of the properties caused by the progressive loss of a
237 fraction of the motoneurons, starting with the least excitable FF motoneurons (Pun
238 et al., 2006; Hegedus et al., 2007, 2008; Martínez-Silva et al., 2018). For this reason,
239 we have split our dataset into three age groups. First, the young adult group (P30–
240 60) corresponds to pre-symptomatic animals, with little to no neuromuscular-
241 junction denervation (denervation starts at >P50 in FF motor units (Pun et al.,
242 2006)). The presymptomatic group (P60–90) corresponds to a group where there
243 are no overt motor symptoms despite a substantial loss of distal axons (Pun et al.,
244 2006) and the beginning of cell death in the spinal cord (Kanning et al., 2009;
245 Lalancette-Hebert et al., 2016). The symptomatic group (P90–120) contains animals
246 showing overt motor symptoms, and who have lost a significant proportion of their
247 motoneurons, particularly in the FF and FR population. Because motoneurons are
248 still intact in the young adult group, changes in electrical properties can be directly
249 interpreted as the direct result of the mutation, rather than the result of a shift in the
250 population average caused by the loss of a fraction of the motoneurons. This age
251 group will therefore be the main focus of the rest of our analysis.

252 **Motoneurons from young adult mutant mice have overly large PICs**

253 In motoneurons, one of the major determinants of excitability are PICs, which
254 were measured in response to a slow (5 mV/s) ramp in voltage-clamp mode. The
255 amplitude of the PIC was measured on the leak-subtracted trace at the point where
256 the downward deflection of the trace was maximal (see Figure 1A–B). We also
257 measured the PIC activation voltage, and the voltage at which the PICs reached their
258 peak.

259 In WT animals, PIC amplitude remained roughly steady during the age period
260 studied (Figure 1C). However, in mSOD1 motoneurons, PIC amplitudes started
261 higher than in WT animals at the youngest stages, then decreased strikingly over
262 time (Figure 1C). When broken down by age groups (Figure 1D), our results show
263 that, in the young adult stage (P30–60), the SOD1 mutation lead to an almost 3×
264 increase in PIC amplitudes compared to WT motoneurons. This increase appears to
265 be a continuation of the trend observed in neonates, where PICs were already
266 increased ~2 fold compared to controls (Quinlan et al., 2011). In the
267 presymptomatic group (P60–90), however, mSOD1 PICs shrunk to the same
268 amplitude as WT motoneurons. At symptomatic stages (P90–120), the trend seen in
269 young animals is reversed: PICs are much smaller in mSOD1 motoneurons
270 compared to WT motoneurons (Table 1).

271 In addition to its effect on PIC amplitude, SOD1 mutation also affected the voltage
272 at which PICs are recruited. The "PIC onset voltage", measured as the voltage at the
273 point where the leak-subtracted motoneuron I-V curve initially begins to curve
274 downward, was hyperpolarized by 10 mV in young mSOD1 mice compared to WT

275 controls (WT: -58.03 ± 6.35 mV, N=19 vs. mSOD1: -69.41 ± 5.71 mV, N=15; $g = -1.83$
276 95%CI $[-2.64--0.78]$; $t(32) = 5.49$, $p = 5.1e-06$), and then slowly increased over time
277 to match the value in WT motoneurons by endstage (Figure 1E). The SOD1 mutation
278 had a similarly large effect on the voltage at which the PIC reached its maximum in
279 young animals (WT: -43.83 ± 4.79 mV, N=19 vs. SOD1: -52.32 ± 4.20 mV, N=15;
280 $g = -1.83$ 95%CI $[-2.63--1.04]$; $t(32) = 5.50$, $p = 4.8e-06$). The peak voltage then
281 increased progressively over time, paralleling the onset voltage (Figure 1F).

282 These profound changes in PIC amplitude and activation voltage would be
283 expected to have an impact on the firing properties of motoneurons. We, therefore,
284 performed current-clamp recordings in the same motoneurons as above. Starting
285 from its natural resting membrane potential, we injected a triangular ramp of
286 current to elicit the repetitive firing of the motoneuron (Figure 2A-B), and
287 measured the voltage threshold for spiking on the first spike triggered by the ramp.
288 In concordance with the hyperpolarization of the PICs, spiking threshold was also
289 hyperpolarized in young animals (WT: -45.35 ± 5.48 mV, N=19 vs. mSOD1:
290 -54.86 ± 5.15 mV, N=14; $g = -1.74$ 95%CI $[-2.53--0.81]$; $t(31) = 5.10$, $p = 1.9e-05$), and
291 increased over time (Figure 1G).

292 **Young adult motoneurons are nonetheless not hyperexcitable**

293 Despite the large alterations in PIC amplitude and activation voltage and the
294 change in the voltage threshold for spiking, the excitability of the motoneurons was
295 remarkably unaffected by the SOD1 mutation, regardless of age. Excitability was
296 quantified using the intensity of the current required to elicit the first spike on the
297 ascending ramp ("recruitment current"). Although the recruitment current

298 decreased over time in mSOD1 animals (Figure 2C), this effect was mostly driven by
299 older animals (Figure 2D). Young adult (P30–60) mutant motoneurons, whose
300 neuromuscular junctions are just starting to be denervated, and pre-symptomatic
301 motoneurons (P60–90), which experience substantial denervation, did not require,
302 on average, less current to reach firing threshold than WT controls (Figure 2D). At
303 symptomatic stages (P90–120), the SOD1 mutation does lead to a decrease in the
304 recruitment current compared to WT animals (Figure 2D), which is probably caused
305 by the degeneration of the high threshold motoneurons at this stage.

306 Neuronal excitability depends not only on how much current is needed to start
307 firing, but also at what frequency the neuron is firing once it is recruited. We
308 quantified the firing frequency of the motoneurons by measuring the slope of the
309 frequency-current relationship. As shown previously (Manuel et al., 2009), most F-I
310 curves, regardless of age and genotype, showed a distinct sub-primary range (SPR)
311 with a steep slope and high variability followed by a linear phase called primary
312 range (PR). We used the "gain" of the motoneuron, i.e. the slope of the F-I curve in
313 the PR, as another measure of excitability of motoneurons. Despite the alterations in
314 PICs in mutant motoneurons, the gain of the motoneuron F-I curves was unaffected
315 by both age and mutation (Figure 2E–F).

316 **Compensatory changes responsible to maintain excitability**

317 The fact that young adult motoneurons are not hyperexcitable despite substantial
318 alterations in the PICs suggests that other compensatory mechanisms are acting to
319 preserve the functional output of the cells. Motoneuron input conductance is an
320 important factor controlling neuron excitability. We estimated the input

321 conductance of mSOD1 and WT motoneurons from the slopes of their I-V
322 relationships around the level of the resting membrane potential (see Figure 1 and
323 Methods). Input conductances of mSOD1 and WT motoneurons are plotted against
324 the age of the animal in Figure 3A. Consistent with the continuous increase in the
325 size of the animals over the age span studied, WT motoneurons exhibit a moderate
326 increase in input conductance in WT motoneurons over time (Figure 3A). On the
327 other hand, mSOD1 motoneurons showed the opposite trend (Figure 3A). Young
328 adult mutant motoneurons had an input conductance almost twice as high as WT
329 controls at P30–P60 (Figure 3B). This increase is relatively greater (~1.7 fold) than
330 that observed in neonatal motoneurons (~1.25 fold) (Quinlan et al., 2011),
331 suggesting that the trend for increased conductance has become stronger as the
332 animal matures into the young adult state. However, by the late pre-symptomatic
333 stage (P60–90), the mutation had no longer any effect on input conductance. Finally,
334 symptomatic (P90–120) mSOD1 motoneurons had a smaller input conductance than
335 WT controls (Figure 3B), but this difference could be due to the degeneration of the
336 largest, high-threshold units at this stage.

337 The increase in input conductance is not the only compensatory change
338 happening in young adult mutant motoneurons. In particular, one would have
339 expected the leftward shift in the activation voltage of PICs seen in these
340 motoneurons to have a profound impact on their firing behavior. This discrepancy
341 can be explained by a parallel hyperpolarization (by almost 10 mV) of the resting
342 membrane potential in young adult mSOD1 motoneurons (Figure 4, P30–60). This
343 effect is still observable at pre-symptomatic stages, but to a lesser degree (Figure 4,

344 P60–90). At symptomatic ages, however, mutant motoneurons had similar resting
345 membrane potentials as WT controls (Figure 4, P90–120).

346 When taking into account this hyperpolarization of the resting membrane
347 potential, the relative values of the voltage threshold for spiking (ΔV_{th} , difference
348 between the voltage threshold and the resting membrane potential), as well as the
349 relative activation voltage of the PICs (ΔV_{PIC}) and the relative voltage at the peak of
350 the PIC (ΔV_{peak}) were all similar between WT and mSOD1 motoneuron regardless of
351 age (Table 1), which suggest that these are the quantities that are homeostatically
352 regulated.

353 **Arms race between PICs and input conductance**

354 Our results show that, during the disease progression, motoneurons are actively
355 engaged in a homeostatic process to maintain their firing output. The ratio of PIC to
356 conductance is a major determinant of net excitability. If these two parameters grow
357 in proportion, then net excitability is likely to stay about the same (Huh et al., 2017).
358 We thus analyzed the relationship between PIC amplitude and input conductance
359 (Figure 5). In the young adult animals (Figure 5A), the majority of the mutant
360 motoneurons are clustered in the upper right-hand corner, with values of both
361 conductances and PIC amplitudes that are outside of the range of WT controls. Yet,
362 the slopes were similar for both groups (ANCOVA, no significant interaction
363 between input conductance and genotype on PIC amplitude, $t(30)=-0.590$, $p=0.560$),
364 and the mutation had only a negligible effect on the relationship between PIC
365 amplitude and conductance (ANCOVA, effect of mutation -0.40 95%CI $[-6.73-5.92]$,
366 $t(30)=-0.130$, $p=0.898$). Therefore the relationship between PIC amplitude and

367 input conductance was the same in WT and mSOD1 mice. This implies that, in these
368 animals, the cells that are abnormally large (large input conductance) also have PICs
369 that have increased in proportion. It is plausible that this process would, by itself,
370 cause undue stress to the cell (Attwell and Laughlin, 2001; Herculano-Houzel, 2011;
371 Howarth et al., 2012), due to the high metabolic demand imposed by their large size,
372 as well as the potential massive influx of calcium caused by their abnormally large
373 PICs. At the pre-symptomatic stages, the WT and mSOD1 populations roughly
374 overlap (Figure 5B). At the symptomatic ages, the situation is reversed, with the
375 appearance of a cluster (N=6) of very small cells with very small PICs (Figure 5C).
376 These results show that the overall initial increase in PIC and conductance
377 amplitudes were driven by the SOD1 mutation generates a sub-population of
378 motoneurons with conductance and PIC amplitudes that are well above the normal,
379 WT range (P30–60). Then, as the disease progresses, the steady reduction in these
380 amplitudes is so strong that by P90–120, some of the surviving cells fall well below
381 the normal range.

382 **Some cells are hypoexcitable and cannot fire repetitively**

383 Despite the remarkable ability of spinal motoneurons to maintain their
384 excitability and firing output demonstrated above, some mSOD1 motoneuron
385 tended to lose their ability to fire repetitively as the disease progressed (Delestrée
386 et al., 2014; Martínez-Silva et al., 2018). Out of the 53 mutant motoneurons
387 recorded, 6 motoneurons could not fire repetitively to current ramps despite still
388 being able to fire a single or a few action potentials to current steps. Figure 6 shows
389 an example of such a motoneuron. Although those cells were not, on average, larger

390 than those that fired repetitively (Figure 6D), non-firing cells were characterized by
391 a very small PIC amplitude (Figure 6E, see also (Huh et al., 2017)). Finally, although
392 some non-firing motoneurons could be recorded in WT mice, non-firing
393 motoneurons appeared, on average, 25 days earlier in mSOD1 mice (Figure 6F).

394 **Other motoneuron properties**

395 Given the large number of electrophysiological parameters measured in each cell
396 (21 per cell), we used Principal Component Analysis (PCA) to analyze the overall
397 behavior of the cells across time and genotype. The first three principal components
398 (PCs) accounted for 67% of the variance in the data. Figure 7A₁₋₃ shows how the
399 first three principal components varied with the age of the animal in mSOD1 and WT
400 mice. For WT mice, all principal components were constant over time (slopes: PC1
401 0.102 AU/week 95%CI[-0.178-0.381], $r^2=0.024$, $p=0.459$; PC2 -0.112 AU/week
402 95%CI[-0.368-0.144], $r^2=0.034$, $p=0.376$; PC3 0.043 AU/week 95%CI[-0.182-
403 0.269], $r^2=0.007$, $p=0.694$). On the other hand, in mSOD1 mice, the first two principal
404 components evolved over time. PC1 started at a higher value than WT mice,
405 decreased over time (slope -0.460 AU/week 95%CI[-0.625--0.295], $r^2=0.450$,
406 $p=1.6e-06$), and became smaller than in WT mice at endstage. PC2 followed the
407 opposite trend. In young mSOD1 animals, PC2 was lower than in WT animals, and
408 then it increased over time (albeit by a very small amount; 0.151 AU/week
409 95%CI[0.006-0.296], $r^2=0.102$, $p=0.042$). Finally, PC3 stayed constant
410 (-0.089 AU/week 95%CI[-0.192-0.013], $r^2=0.074$, $p=0.086$) and indistinguishable
411 from WT. Higher principal components did not show any dependency on age or
412 genotype (not shown).

413 The opposite behavior of PC1 and PC2 in mSOD1 mice indicates that several
414 features are anti-correlated. PC1 was strongly positively correlated to input
415 conductance, as well as most current measurements (PIC amplitude, recruitment
416 current, etc.) (Figure 7B), which were also the features that were increased the most
417 in young adult mSOD1 vs. WT animals (Figure 7C, top rows). On the other hand, PC2
418 was more strongly correlated to voltage measurements (voltage threshold, PIC peak
419 voltage, PIC onset voltage, resting membrane potential; Figure 7B), which were
420 features that were strongly decreased in young adult mSOD1 vs. WT (Figure 7C,
421 bottom rows). Overall, PCA clearly highlights two sets of features that evolve in
422 opposite direction over time, presumably to compensate for one another in order to
423 maintain neuronal excitability as close to normal as possible.

424 Discussion

425 In this paper, we studied how motoneuron electrical properties evolve over the
426 time course of ALS, focusing particularly on the persistent inward currents (PICs).
427 We show that, in young adult mutant mice, before and up to the time when motor
428 unit denervation is just starting, PICs are abnormally large compared to controls.
429 This increase in PIC amplitude is accompanied by a parallel increase in motoneuron
430 input conductance with the net effect that the excitability of the cells remains
431 normal. Later, while the animals remain pre-symptomatic but denervation has
432 begun, motoneuron properties return to normal levels. Finally, in symptomatic
433 animals, mutant motoneurons tend to have smaller input conductance and smaller

434 recruitment current, which is most likely due to the death of the largest, low
435 threshold cells at this stage.

436 **Homeostatic regulation of motoneuron output**

437 Although ALS is classically considered an adult-onset disease, we know from
438 earlier studies of motoneurons in animal models of ALS that the change in
439 motoneurons' intrinsic excitability is the first sign to be seen in the pathogenesis,
440 long before any overt motor deficits manifest. Hyperexcitability is observed in
441 cultured E13 spinal motoneurons (Kuo et al., 2004), E15 cortical motoneurons (Pieri
442 et al., 2009), E17.5 spinal motoneurons (Martin et al., 2013 p.20), as well as early
443 postnatal hypoglossal motoneurons (van Zundert et al., 2008). Consequently, the
444 motor system in general, and motoneurons in particular, must exhibit remarkable
445 capability for homeostatic regulation to maintain a quasi-normal motor output until
446 overt symptoms appear, but there are many combinations of intrinsic properties
447 that can produce the same firing pattern (Marder and Goaillard, 2006). In neonatal
448 mSOD1 mice, the majority of motoneurons exhibited normal excitability (based on
449 recruitment current and F-I gain), although the most resistant population of
450 motoneuron seem to retain some hyperexcitability (Quinlan et al., 2011; Leroy et al.,
451 2014). Yet, PICs were almost twice as large in mutant compared to WT neonatal
452 motoneurons (Quinlan et al., 2011). This increased PIC amplitude was seemingly
453 compensated by a parallel increase in input conductance (Quinlan et al., 2011). In
454 adults, this trend seems to continue, particularly in the young adult age group.
455 Global analysis of our dataset using PCA shows that, generally speaking, currents
456 tend to be much bigger in young adult mSOD1 mice compared to WT (we observe an

457 almost 3× increase in PIC amplitude, accompanied by an almost 2× increase in input
458 conductance), which then tend to decrease over time. This increase is accompanied
459 by a hyperpolarization of the PIC onset and peak voltages, but which are
460 compensated by a commensurate hyperpolarization of the resting membrane
461 potential. These trends with disease progression from the embryonic state through
462 the development of severe symptoms are summarized in Figure 8. An overall
463 pattern of oscillations is evident, with the PIC oscillations tending to increase
464 excitability but the conductance and rest potential oscillations tending to reduce it.

465 The properties of the motoneurons seem to normalize at the late pre-
466 symptomatic stage (P60–90), but it is unclear whether this is due to changes in the
467 homeostatic pathways involved, or whether it is caused by the start of the
468 degeneration process in the most vulnerable motoneurons. At symptomatic stages,
469 motoneurons appear to be hyper-excitable. They have, on average, a smaller input
470 conductance (Figure 3), and smaller recruitment current (Figure 2), but that most
471 likely reflect the fact that the largest cells have degenerated by this age, and that the
472 remaining cells may have shrunk (see below, and Dukkupati et al., 2018). In addition,
473 it should be noted that a small but growing number of cells become incapable of
474 firing repetitively at this stage (Delestrée et al., 2014; Martínez-Silva et al., 2018).

475 **The hidden cost of excitability homeostasis**

476 Although the degeneration of motoneurons in ALS constitutes a failure in cell
477 homeostasis, our results show that, throughout the “silent”, presymptomatic phase
478 of ALS, motoneurons are actively engaged in a highly successful homeostatic process
479 to maintain their firing output, and thereby producing a normal motor behavior.

480 The driving force behind this homeostatic process remains mysterious. Although
481 it is commonly agreed that intracellular calcium plays a major role in this process
482 (Turrigiano et al., 1994; O’Leary et al., 2010; O’Leary and Wyllie, 2011), this calcium
483 can enter the cell through various channels (e.g. synaptic receptors, voltage-
484 dependent calcium channels) and the location and pattern of that calcium signal
485 could potentially have distinct downstream targets. We demonstrated here that
486 motoneurons can maintain a normal firing output through most of the pre-
487 symptomatic phase of the disease in response to current injected through the
488 microelectrode. Yet, during behavior, motoneurons are activated through synaptic
489 inputs, most of which are impinging on the dendritic tree. Bączyk, Ouali Alami et al.
490 (2020) have recently demonstrated that excitatory synaptic inputs are depressed in
491 pre-symptomatic mSOD1 mice. Excitability homeostasis, therefore, cannot be
492 restricted to the intrinsic properties of motoneurons, but potentially involve the
493 whole sensorimotor network. Indeed, in the motor cortex, although several cell
494 types (including corticospinal pyramidal cells) were found to be intrinsically
495 hyperexcitable in symptomatic mSOD1 mice, the activity of corticospinal pyramidal
496 neurons during behavior (measured by two-photon calcium imaging during head-
497 fixed locomotion) was indistinguishable from controls (Kim et al., 2017). Whether
498 network-level homeostasis and intrinsic excitability homeostasis are parallel,
499 independent, processes, or whether one precedes and drives the other remains to be
500 investigated.

501 Whatever the case may be, the process by which the cells maintain the firing
502 output could, by itself, be a major source of stress for the cells. We do not know

503 whether the cells increase their conductance to compensate for the fast increase in
504 PICs or *vice versa*, but the result is the appearance of cells with both input
505 conductance and PIC amplitudes outside of the normal range (Figure 5A). The
506 increase in input conductance could be due to the insertion of more channels in the
507 membrane. However, direct measurements of soma sizes have revealed that pre-
508 symptomatic mutant cells are physically larger than controls (Shoenfeld et al., 2014;
509 Dukkupati et al., 2018). This increase in size, coupled with the larger calcium entry in
510 the cells due to the larger PICs (which are in part calcium-mediated (Li and
511 Bennett, 2003)), is bound to cause undue metabolic stress on those cells that are
512 outside of the normal range (Attwell and Laughlin, 2001), even though cells manage
513 to maintain a normal output. If we assume that all motoneurons experience the
514 same shift in their properties, then Fast Fatigable (FF) motoneurons, which are the
515 cells with the largest input conductance, and the largest PICs in normal conditions
516 (Lee and Heckman, 1998; Huh et al., 2017), are likely to be the cells that are the
517 further out of the normal range. This might explain why they are the most
518 vulnerable to ALS (Pun et al., 2006; Hegedus et al., 2007, 2008).

519 As the disease progresses, those large, vulnerable cells become the first
520 motoneurons that will embark on a degeneration pathway (Saxena et al., 2009,
521 2013; Martínez-Silva et al., 2018), and will lose their ability to fire repetitively
522 (Martínez-Silva et al., 2018). This early loss of the large cells is consistent with stress
523 induced by aberrantly large conductances and PICs. This loss is also likely the
524 primary reason why motoneurons appear to recover normal properties at late pre-
525 symptomatic stages. Nevertheless, it is probable that all motoneurons, regardless of

526 type, experience this form of stress. Interestingly, we observed that some of the
527 smallest motoneurons, which are the most resistant to the disease, appear to shrink
528 in the oldest animals (Figure 5C), consistent with anatomical observations (Kiernan
529 and Hudson, 1991; Dukkipati et al., 2018). At this point, it is unclear whether this
530 shrinkage is a pathological feature or a strong homeostatic effort by the surviving
531 motoneurons to counteract the stress generated by their initial hypertrophy.

532 **Hyper-vigilant homeostasis**

533 Mitchell and colleagues have recently performed meta-analyses of data obtained
534 from many studies on multiple cellular properties, which revealed patterns of
535 oscillations as the disease progressed, suggesting the existence of high feedback
536 gains for homeostatic processes (Mitchell and Lee, 2012; Irvin et al., 2015). Several
537 aspects of our results are consistent with this “hyper-vigilant” homeostasis
538 hypothesis. Similar oscillatory patterns are present in our results, as illustrated in
539 Figure 8. Although the cells are successful at maintaining their net excitability
540 constant, this is achieved at the cost of excessively high amplitudes for conductances
541 and PICs. These large amplitude changes lead to the appearance of groups of cells
542 that are first well above the normal range of properties, followed by an over-
543 reaction where some cells end up well below the normal range. This behavior fits
544 well with the “hyper-vigilant” model (Irvin et al., 2015), but a direct test of the
545 hyper-vigilant homeostasis hypothesis will require quantitative comparisons of the
546 responses of ALS and WT motoneurons to controlled homeostatic challenges.

547 **Comparison with previous studies**

548 Previous studies in adult SOD1 mice have suggested that spinal motoneurons
549 became hyperexcitable (Meehan et al., 2010; Jensen et al., 2020). The most recent
550 study uses the same SOD1(G93A) and same anesthetics as the present study, but has
551 focused on two fairly advanced time points (~P75 and ~P115). They have observed
552 an increase in input resistance (decrease in input conductance) between WT and
553 mSOD1 mice at P115, which is consistent with our results, and is probably due to
554 the loss of the largest motoneurons at this stage. They also reported a decrease in
555 input conductance at P75, which we did not find in the present sample. The cause
556 for this discrepancy remains unknown, but is compatible with the early death of the
557 largest motoneurons. In their dataset, this decrease in conductance was associated
558 with an apparent hyperexcitability: the recruitment current was lower and the F-I
559 curve was steeper. However, their use of a low DCC switching rate (3 kHz, compared
560 to 6–8 kHz used here) may have distorted the firing properties of their cells and led
561 to an overestimation of their excitability (Manuel, 2020 in press).

562 We have previously studied the properties of motoneurons in the same
563 SOD1(G93A) mouse model of ALS (Delestrée et al., 2014; Martínez-Silva et al., 2018)
564 but have mainly focused on a short period just at the onset of denervations (P45–
565 55). Although that time point partly overlaps with the present young adult stage, we
566 had not detected differences in input conductances (Martínez-Silva et al., 2018).
567 This might be because the difference in input conductance is largest at earlier time
568 points (Figure 3). Indeed, the difference is gone at P60–90, and we did report an
569 increase in input conductance in an earlier series of experiments, which was more

570 pronounced in younger animals (Delestrée et al., 2014). Similarly, we did not detect
571 a difference in resting membrane potential in the Martínez-Silva et al. (2018) study.
572 Again, the discrepancy could be due to the difference in the distributions of the ages
573 of the animals studied. The precise reason for this difference remains, however,
574 unknown and warrants further study.

575 Since input conductance is dependent on motoneuron size (Burke, 1981;
576 Heckman and Enoka, 2012), our present results are consistent with anatomical
577 studies that have measured soma sizes in mSOD1 mice. In young adult animals,
578 motoneurons are markedly larger in mSOD1 mice compared to WT animals
579 (particularly in males)(Shoenfeld et al., 2014; Dukkipati et al., 2018). At
580 symptomatic stages, however, the situation is reversed and the remaining
581 motoneurons appear to have shrunk below the size of the smallest motoneurons in
582 WT mice (Dukkipati et al., 2018).

583 In the present study, we recorded only 13 motoneurons out of 103 (7/50 WT and
584 6/53 mSOD1) that were unable to fire repetitively, contrary to our previous study
585 where we showed that a large proportion of vulnerable motoneurons became
586 hypoexcitable before the onset of denervation (P45–55, Martínez-Silva et al., 2018).
587 This discrepancy could be explained by the experimental constraints of the present
588 study. Indeed, obtaining stable voltage-clamp recordings mice in vivo is quite a
589 challenge, requiring electrodes able to pass substantial amounts of current and
590 motoneuron able to withstand the protocol. Since we have only included for analysis
591 cells in which both the voltage-clamp and current-clamp protocols were completed

592 successfully, we hypothesize that we may have biased our sample towards the
593 healthiest cells that have yet to take the path of degeneration.

594 **Limitations**

595 The results presented here have been collected on the SOD1(G93A) mouse model
596 of ALS, a model that has attracted criticisms due to it being an overexpression
597 model, and its failure to bring seemingly promising therapies to the clinic (Philips
598 and Rothstein, 2015). Nevertheless, some parallel with other studies suggests that
599 our results could be extended to other models. First, Meehan et al. (2010) have
600 studied an unrelated mSOD1(G127X) model and have shown that although the net
601 excitability of the motoneurons was not affected by the mutation, there were
602 nonetheless signs of increased PICs in these motoneurons. Second, we observed
603 that, in late symptomatic animals, some cells exhibited a very small input
604 conductance, well below the normal range at this age, suggesting that these cells
605 actually shrank. This observation matches morphological measurements in mSOD1
606 mice (Dukkipati et al., 2018), but also observations from sporadic human patients
607 (Kiernan and Hudson, 1991).

608 We demonstrated a remarkably successful homeostatic control of motoneuron
609 firing, that we can attribute to commensurate changes in PICs and input
610 conductance. However, it is likely that other currents are also implicated in this
611 process (Marder and Goaillard, 2006). Limitations inherent to in vivo
612 electrophysiology prevent us from isolating many different currents and further in
613 vitro investigations in adults (Jiang and Heckman, 2006; Mitra and Brownstone,

614 2011; Jiang et al., 2017; Bhumbra and Beato, 2018) are warranted to shed more light
615 on the panoply of channels involved in this process.

616 **Conclusion**

617 Overall, our results show homeostasis for net excitability in mutant SOD1
618 motoneurons is remarkably strong in the presymptomatic state. This success
619 however comes at a cost of large compensatory changes in basic electrical
620 properties. These results support the hypothesis that ALS is not due to a single
621 specific root cause but instead caused by an inherent instability at the system-level
622 (Mitchell and Lee, 2012), possibly caused by a “hyper-vigilant” homeostatic system
623 in motoneurons. Initial perturbations in the electrical properties of motoneurons
624 would be overcompensated for, leading to new sources of stress, which, in turn,
625 would be overcorrected, and so forth until the metabolic burden becomes too high
626 to sustain for the motoneuron. FF motoneurons have higher metabolic needs (Le
627 Masson et al., 2014) and lower calcium-buffering capabilities (Grosskreutz et al.,
628 2010) in the first place, which make them particularly vulnerable to this vicious
629 cycle.

630 **Data availability**

631 Data files and a computational notebook allowing reproducing the analysis and
632 figures of this article are provided at the URL:

633 <https://doi.org/10.5281/zenodo.3831946>

634 **References**

- 635 Attwell D, Laughlin SB (2001) An Energy Budget for Signaling in the Grey Matter of
636 the Brain. *J Cereb Blood Flow Metab* 21:1133–1145 DOI: 10.1097/00004647-
637 200110000-00001.
- 638 Bączyk M, Ouali Alami N, Delestrée N, Martinot C, Tang L, Comisso B, Bayer D,
639 Doisne N, Frankel W, Manuel M, Roselli F, Zytnicki D (2020) Synaptic
640 restoration by cAMP/PKA drives activity-dependent neuroprotection to
641 motoneurons in ALS. *J Exp Med* 217 DOI: 10.1084/jem.20191734.
- 642 Bernard C (2019) Changing the Way We Report, Interpret, and Discuss Our Results
643 to Rebuild Trust in Our Research. *eNeuro* 6 DOI: 10.1523/ENEURO.0259-
644 19.2019.
- 645 Bhumbra GS, Beato M (2018) Recurrent excitation between motoneurons
646 propagates across segments and is purely glutamatergic. *PLOS Biol*
647 16:e2003586 DOI: 10.1371/journal.pbio.2003586.
- 648 Brownstone RM, Lancelin C (2018) Escape from homeostasis: spinal microcircuits
649 and progression of amyotrophic lateral sclerosis. *J Neurophysiol* 119:1782–
650 1794 DOI: 10.1152/JN.00331.2017.
- 651 Burke RE (1981) Motor units: anatomy, physiology, and functional organization. In:
652 Handbook of physiology. The nervous system. Motor control., pp 345–422.
653 American Physiological Society.
- 654 Cumming G (2012) Understanding the new statistics: effect sizes, confidence
655 intervals, and meta-analysis. New York: Routledge, Taylor & Francis Group.
- 656 Delestrée N, Manuel M, Iglesias C, Elbasiouny SM, Heckman CJ, Zytnicki D (2014)
657 Adult spinal motoneurons are not hyperexcitable in a mouse model of
658 inherited amyotrophic lateral sclerosis. *J Physiol* 592:1687–1703 DOI:
659 10.1113/JPHYSIOL.2013.265843.
- 660 Dukkipati SS, Garrett TL, Elbasiouny SM (2018) The vulnerability of spinal
661 motoneurons and soma size plasticity in a mouse model of amyotrophic lateral
662 sclerosis. *J Physiol* 596:1723–1745 DOI: 10.1113/JP275498.
- 663 Grosskreutz J, van den Bosch L, Keller BU (2010) Calcium dysregulation in
664 amyotrophic lateral sclerosis. *Cell Calcium* 47:165–174 DOI:
665 10.1016/j.ceca.2009.12.002.
- 666 Heckman CJ, Enoka RM (2012) Motor Unit. *Compr Physiol* 2:2629–2682 DOI:
667 10.1002/cphy.c100087.
- 668 Hedges LV (2016) Distribution Theory for Glass's Estimator of Effect size and
669 Related Estimators: *J Educ Stat* DOI: 10.3102/10769986006002107.
- 670 Hegedus J, Putman CT, Gordon T (2007) Time course of preferential motor unit loss
671 in the SOD1 G93A mouse model of amyotrophic lateral sclerosis. *Neurobiol Dis*
672 28:154–164 DOI: 10.1016/j.nbd.2007.07.003.
- 673 Hegedus J, Putman CT, Tyreman N, Gordon T (2008) Preferential motor unit loss in
674 the SOD1 G93A transgenic mouse model of amyotrophic lateral sclerosis. *J*
675 *Physiol* 586:3337–3351 DOI: 10.1113/jphysiol.2007.149286.

- 676 Herculano-Houzel S (2011) Scaling of Brain Metabolism with a Fixed Energy Budget
677 per Neuron: Implications for Neuronal Activity, Plasticity and Evolution. *PLoS*
678 *ONE* 6 DOI: 10.1371/journal.pone.0017514.
- 679 Ho J, Tumkaya T, Aryal S, Choi H, Claridge-Chang A (2019) Moving beyond P values:
680 data analysis with estimation graphics. *Nat Methods* 16:565–566 DOI:
681 10.1038/s41592-019-0470-3.
- 682 Howarth C, Gleeson P, Attwell D (2012) Updated Energy Budgets for Neural
683 Computation in the Neocortex and Cerebellum. *J Cereb Blood Flow Metab*
684 32:1222–1232 DOI: 10.1038/jcbfm.2012.35.
- 685 Huh S, Siripuram R, Lee RH, Turkin VV, O’Neill D, Hamm TM, Heckman CJ, Manuel M
686 (2017) PICs in motoneurons do not scale with the size of the animal: a possible
687 mechanism for faster speed of muscle contraction in smaller species. *J*
688 *Neurophysiol* 118:93–102 DOI: 10.1152/JN.00045.2017.
- 689 Hunter JD (2007) Matplotlib: A 2D Graphics Environment. *Comput Sci Eng* 9:90–95
690 DOI: 10.1109/MCSE.2007.55.
- 691 Ilieva H, Polymenidou M, Cleveland DW (2009) Non-cell autonomous toxicity in
692 neurodegenerative disorders: ALS and beyond. *J Cell Biol* 187:761–772 DOI:
693 10.1083/jcb.200908164.
- 694 Irvin CW, Kim RB, Mitchell CS (2015) Seeking homeostasis: temporal trends in
695 respiration, oxidation, and calcium in SOD1 G93A Amyotrophic Lateral
696 Sclerosis mice. *Front Cell Neurosci* 9:248 DOI: 10.3389/FNCEL.2015.00248.
- 697 Jensen DB, Kadlecova M, Allodi I, Meehan CF (2020) Spinal motoneurons are
698 intrinsically more responsive in the adult G93A SOD1 mouse model of
699 amyotrophic lateral sclerosis. *J Physiol* 598:4385–4403 DOI:
700 10.1113/JP280097.
- 701 Jiang MC, Adimula A, Birch D, Heckman CJ (2017) Hyperexcitability in synaptic and
702 firing activities of spinal motoneurons in an adult mouse model of
703 amyotrophic lateral sclerosis. *Neuroscience* 362:33–46 DOI:
704 10.1016/j.neuroscience.2017.08.041.
- 705 Jiang MC, Heckman CJ (2006) In vitro sacral cord preparation and motoneuron
706 recording from adult mice. *J Neurosci Off J Soc Neurosci* 156:31–36.
- 707 Johnson MD, Heckman CJ (2010) Interactions between focused synaptic inputs and
708 diffuse neuromodulation in the spinal cord. *Ann N Y Acad Sci* 1198:35–41 DOI:
709 10.1111/J.1749-6632.2010.05430.X.
- 710 Kanning KC, Kaplan A, Henderson CE (2009) Motor neuron diversity in development
711 and disease. *Annu Rev Neurosci* 33:409–440.
- 712 Kiernan JA, Hudson AJ (1991) Changes in Sizes of Cortical and Lower Motor Neurons
713 in Amyotrophic Lateral Sclerosis. *Brain* 114:843–853 DOI:
714 10.1093/brain/114.2.843.
- 715 Kim J, Hughes EG, Shetty AS, Arlotta P, Goff LA, Bergles DE, Brown SP (2017)
716 Changes in the Excitability of Neocortical Neurons in a Mouse Model of
717 Amyotrophic Lateral Sclerosis Are Not Specific to Corticospinal Neurons and
718 Are Modulated by Advancing Disease. *J Neurosci Off J Soc Neurosci* 37:9037–
719 9053 DOI: 10.1523/JNEUROSCI.0811-17.2017.
- 720 Kuo JJ, Schonewille M, Siddique T, Schults ANA, Fu R, Bär PR, Anelli R, Heckman CJ,
721 Kroese ABA (2004) Hyperexcitability of cultured spinal motoneurons from

- 722 presymptomatic ALS mice. *J Neurophysiol* 91:571–575 DOI:
723 10.1152/jn.00665.2003.
- 724 Lalancette-Hebert M, Sharma A, Lyashchenko AK, Shneider NA (2016) Gamma
725 motor neurons survive and exacerbate alpha motor neuron degeneration in
726 ALS. *Proc Natl Acad Sci U S A* 113:E8316–E8325 DOI:
727 10.1073/pnas.1605210113.
- 728 Le Masson G, Przedborski S, Abbott LF (2014) A Computational Model of Motor
729 Neuron Degeneration. *Neuron* 83:758–760 DOI:
730 10.1016/j.neuron.2014.07.001.
- 731 Lee RH, Heckman CJ (1998) Bistability in spinal motoneurons in vivo: systematic
732 variations in persistent inward currents. *J Neurophysiol* 80:583–593.
- 733 Leitner M, Menzies S, Lutz C (2009) Working with ALS Mice. The Jackson
734 Laboratory.
- 735 Leroy F, Lamotte d’Incamps B, Imhoff-Manuel RD, Zytnicki D (2014) Early intrinsic
736 hyperexcitability does not contribute to motoneuron degeneration in
737 amyotrophic lateral sclerosis. *eLife* 3 DOI: 10.7554/eLife.04046.
- 738 Li Y, Bennett DJ (2003) Persistent sodium and calcium currents cause plateau
739 potentials in motoneurons of chronic spinal rats. *J Neurophysiol* 90:857–869.
- 740 Makin TR, Orban de Xivry J-J (2019) Ten common statistical mistakes to watch out
741 for when writing or reviewing a manuscript Rodgers P, Parsons N, Holmes N,
742 eds. *eLife* 8:e48175 DOI: 10.7554/eLife.48175.
- 743 Manuel M (2020) Sub-optimal Discontinuous Current-Clamp switching rates lead to
744 deceptive mouse neuronal firing. *bioRxiv*:2020.08.13.250134 DOI:
745 10.1101/2020.08.13.250134.
- 746 Manuel M, Heckman CJ (2011) Adult mouse motor units develop almost all of their
747 force in the subprimary range: a new all-or-none strategy for force
748 recruitment? *J Neurosci* 31:15188–15194 DOI: 10.1523/JNEUROSCI.2893-
749 11.2011.
- 750 Manuel M, Iglesias C, Donnet M, Leroy F, Heckman CJ, Zytnicki D (2009) Fast
751 kinetics, high-frequency oscillations, and subprimary firing range in adult
752 mouse spinal motoneurons. *J Neurosci* 29:11246–11256 DOI:
753 10.1523/JNEUROSCI.3260-09.2009.
- 754 Marder E, Goaillard J-M (2006) Variability, compensation and homeostasis in
755 neuron and network function. *Nat Rev Neurosci* 7:563–574 DOI:
756 10.1038/nrn1949.
- 757 Martin E, Cazenave W, Cattaert D, Branchereau P (2013) Embryonic alteration of
758 motoneuronal morphology induces hyperexcitability in the mouse model of
759 amyotrophic lateral sclerosis. *Neurobiol Dis* 54:116–126 DOI:
760 10.1016/j.nbd.2013.02.011.
- 761 Martínez-Silva M de L, Imhoff-Manuel RD, Sharma A, Heckman C, Shneider NA,
762 Roselli F, Zytnicki D, Manuel M (2018) Hypoexcitability precedes denervation
763 in the large fast-contracting motor units in two unrelated mouse models of ALS
764 Rubin LL, ed. *eLife* 7:e30955 DOI: 10.7554/ELIFE.30955.
- 765 McKinney W (2011) pandas: a foundational Python library for data analysis and
766 statistics. *Python High Perform Sci Comput* 14.

- 767 Meehan CF, Moldovan M, Marklund SL, Graffmo KS, Nielsen JB, Hultborn H (2010)
768 Intrinsic properties of lumbar motor neurones in the adult G127insTGGG
769 superoxide dismutase-1 mutant mouse in vivo: evidence for increased
770 persistent inward currents. *Acta Physiol Oxf Engl* 200:361–376 DOI:
771 10.1111/j.1748-1716.2010.02188.x.
- 772 Michel MC, Murphy TJ, Motulsky HJ (2020) New Author Guidelines for Displaying
773 Data and Reporting Data Analysis and Statistical Methods in Experimental
774 Biology. *Mol Pharmacol* 97:49–60 DOI: 10.1124/mol.119.118927.
- 775 Mitchell CS, Lee RH (2012) Dynamic Meta-Analysis as a Therapeutic Prediction Tool
776 for Amyotrophic Lateral Sclerosis. In: *Amyotrophic Lateral Sclerosis* (Maurer
777 M, ed). InTech. DOI: 10.5772/32384.
- 778 Mitra P, Brownstone RM (2011) An in vitro spinal cord slice preparation for
779 recording from lumbar motoneurons of the adult mouse. *J Neurophysiol*
780 107:728–741 DOI: 10.1152/JN.00558.2011.
- 781 O'Leary T, Rossum MCW van, Wyllie DJA (2010) Homeostasis of intrinsic excitability
782 in hippocampal neurones: dynamics and mechanism of the response to chronic
783 depolarization. *J Physiol* 588:157–170 DOI: 10.1113/jphysiol.2009.181024.
- 784 O'Leary T, Wyllie DJA (2011) Neuronal homeostasis: time for a change? *J Physiol*
785 589:4811–4826 DOI: 10.1113/jphysiol.2011.210179.
- 786 Pedregosa F, Varoquaux G, Gramfort A, Michel V, Thirion B, Grisel O, Blondel M,
787 Prettenhofer P, Weiss R, Dubourg V, Vanderplas J, Passos A, Cournapeau D,
788 Brucher M, Perrot M, Duchesnay E (2011) Scikit-learn: Machine Learning in
789 Python. *J Mach Learn Res* 12:2825–2830.
- 790 Philips T, Rothstein JD (2015) Rodent Models of Amyotrophic Lateral Sclerosis. *Curr*
791 *Protoc Pharmacol Editor Board SJ Enna Ed--Chief AI* 69:5.67.1-5.67.21 DOI:
792 10.1002/0471141755.ph0567s69.
- 793 Pieri M, Carunchio I, Curcio L, Mercuri NB, Zona C (2009) Increased persistent
794 sodium current determines cortical hyperexcitability in a genetic model of
795 amyotrophic lateral sclerosis. *Exp Neurol* 215:368–379 DOI:
796 10.1016/j.expneurol.2008.11.002.
- 797 Pun S, Santos AF, Saxena S, Xu L, Caroni P (2006) Selective vulnerability and pruning
798 of phasic motoneuron axons in motoneuron disease alleviated by CNTF. *Nat*
799 *Neurosci* 9:408–419 DOI: 10.1038/nn1653.
- 800 Quinlan KA, Schuster JE, Fu R, Siddique T, Heckman CJ (2011) Altered postnatal
801 maturation of electrical properties in spinal motoneurons in a mouse model of
802 amyotrophic lateral sclerosis. *J Physiol* 589:2245–2260.
- 803 Rolfe DF, Brown GC (1997) Cellular energy utilization and molecular origin of
804 standard metabolic rate in mammals. *Physiol Rev* 77:731–758 DOI:
805 10.1152/physrev.1997.77.3.731.
- 806 Rosen DR, Siddique T, Patterson D, Figlewicz DA, Sapp P, Hentati A, Donaldson D,
807 Goto J, O'Regan JP, Deng H-X (1993) Mutations in Cu/Zn superoxide dismutase
808 gene are associated with familial amyotrophic lateral sclerosis. *Nature* 362:59–
809 62 DOI: 10.1038/362059a0.
- 810 Saxena S, Cabuy E, Caroni P (2009) A role for motoneuron subtype-selective ER
811 stress in disease manifestations of FALS mice. *Nat Neurosci* 12:627–636 DOI:
812 10.1038/nn.2297.

- 813 Saxena S, Roselli F, Singh K, Leptien K, Julien J, Gros-louis F, Caroni P (2013)
814 Neuroprotection through Excitability and mTOR Required in ALS Motoneurons
815 to Delay Disease and Extend Survival. *Neuron* 80:80–96 DOI:
816 10.1016/j.neuron.2013.07.027.
- 817 Seabold S, Perktold J (2010) statsmodels: Econometric and statistical modeling with
818 python. In: 9th Python in Science Conference DOI: 10.25080/Majora-
819 92bf1922-011.
- 820 Sekerli M, Del Negro CA, Lee RH, Butera RJ (2004) Estimating action potential
821 thresholds from neuronal time-series: new metrics and evaluation of
822 methodologies. *IEEE Trans Biomed Eng* 51:1665–1672 DOI:
823 10.1109/TBME.2004.827531.
- 824 Shoenfeld L, Westenbroek RE, Fisher E, Quinlan K a, Tysseling VM, Powers RK,
825 Heckman CJ, Binder MD (2014) Soma size and Cav1.3 channel expression in
826 vulnerable and resistant motoneuron populations of the SOD1G93A mouse
827 model of ALS. *Physiol Rep* 2:e12113 DOI: 10.14814/phy2.12113.
- 828 Turrigiano G, Abbott LF, Marder E (1994) Activity-dependent changes in the
829 intrinsic properties of cultured neurons. *Science* 264:974–977 DOI:
830 10.1126/science.8178157.
- 831 van Zundert B, Peuscher MH, Hynynen M, Chen A, Neve RL, Brown RH, Constantine-
832 Paton M, Bellingham MC (2008) Neonatal neuronal circuitry shows
833 hyperexcitable disturbance in a mouse model of the adult-onset
834 neurodegenerative disease amyotrophic lateral sclerosis. *J Neurosci Off J Soc*
835 *Neurosci* 28:10864–10874 DOI: 10.1523/JNEUROSCI.1340-08.2008.
- 836 Virtanen P et al. (2020) SciPy 1.0: fundamental algorithms for scientific computing
837 in Python. *Nat Methods*:1–12 DOI: 10.1038/s41592-019-0686-2.
- 838 Waskom M et al. (2020) mwaskom/seaborn: v0.10.0 (January 2020). Zenodo. DOI:
839 10.5281/zenodo.3629446.
- 840 Wasserstein RL, Schirm AL, Lazar NA (2019) Moving to a World Beyond “ $p < 0.05$.”
841 *Am Stat* 73:1–19 DOI: 10.1080/00031305.2019.1583913.
- 842 Welch BL (1947) The generalisation of student’s problems when several different
843 population variances are involved. *Biometrika* 34:28–35 DOI:
844 10.1093/biomet/34.1-2.28.
- 845

846 **Figure legends**

847 **Figure 1: PIC amplitude is larger is young adult mSOD1 mice**

848 **A.** Example of a PIC recording from a P43 WT mouse. The green bottom trace is
849 the ascending part of the voltage ramp. The top blue trace is the raw current. The
850 dashed line shows the leak current estimated by fitting a straight line in the
851 subthreshold potential region, and which is used to measure the input conductance

852 of the cell. The leak-subtracted current trace is obtained by subtracting the leak
853 current from the raw current trace. The dash-dotted lines show some of the
854 measurements: *PIC amp.*: PIC amplitude, measured at the point of largest deflection
855 on the leak-subtracted trace; V_{onset} : voltage at which the PICs start to activate; V_{peak} :
856 voltage at which PICs reach their maximum. **B.** Example of a PIC recording from a
857 P35 mSOD1 mouse. Same organization as in A. **C.** Plot of the amplitude of the PICs
858 (in nA) vs. age in WT (blue square) and mSOD1 mice (red diamonds). The solid lines
859 correspond to the linear regression lines with 95% confidence intervals (shaded
860 areas). WT: slope=0.12 nA/week 95%CI[-0.068-0.32], $r^2=0.034$ ($p=0.2$); SOD1:
861 slope=-0.45 nA/week 95%CI[-0.64--0.25], $r^2=0.29$ ($p=3.4e-05$). **D.** Breakdown of
862 the difference in PIC amplitude between WT and mSOD1 animals by age groups.
863 P30-60 WT: 2.30 ± 2.17 nA, N=19 vs. mSOD1: 6.73 ± 3.28 nA, N=15; $g=1.59$
864 95%CI[0.63-2.45]; $t(32)=-4.50$, $p=0.00016$. P60-90 WT: 2.47 ± 1.69 nA, N=16 vs.
865 mSOD1: 2.75 ± 2.40 nA, N=24; $g=0.12$ 95%CI[-0.53-0.65]; $t(38)=-0.42$, $p=0.67$. P90-
866 120 WT: 4.12 ± 3.69 nA, N=15 vs. mSOD1: 1.90 ± 1.78 nA, N=14; $g=-0.74$
867 95%CI[-1.26-0.01]; $t(27)=2.08$, $p=0.05$. **E.** Evolution of the membrane potential at
868 which the PICs start to activate (PIC onset voltage) vs. age. WT:
869 slope=-0.33 mV/week 95%CI[-0.77-0.11], $r^2=0.045$ ($p=0.14$). SOD1:
870 slope=0.91 mV/week 95%CI[0.41-1.4], $r^2=0.21$ ($p=0.00063$). **F.** Evolution of the
871 membrane potential at which the PICs reach their peak (PIC peak voltage) vs. age.
872 WT: slope=-0.29 mV/week 95%CI[-0.73-0.16], $r^2=0.034$ ($p=0.2$). SOD1:
873 slope=0.68 mV/week 95%CI[0.28-1.1], $r^2=0.18$ ($p=0.0014$). **G.** Evolution of the
874 voltage threshold for spiking (measure in current-clamp mode) vs. age. WT:

875 slope= -0.14 mV/week 95%CI $[-0.57-0.28]$, $r^2=0.0096$ ($p=0.5$). SOD1:

876 slope= 0.77 mV/week 95%CI $[0.34-1.2]$, $r^2=0.23$ ($p=0.0007$).

877 **Figure 2. Mutant motoneurons are not hyperexcitable**

878 **A.** Example of the response of a P43 WT mouse (same motoneuron as in Figure
879 1A) to a triangular ramp of current. From bottom to top, traces are: injected current,
880 membrane potential, and instantaneous firing frequency. The dash-dotted lines
881 show some of the measurements: $I_{recruit}$: current intensity at which the motoneuron
882 starts to fire; $I_{derecruit}$: de-recruitment current; ΔI : difference between the de-
883 recruitment and recruitment currents; $I_{trans. SPR/PR}$: the current at the transition
884 between sub-primary range and primary range; $F-I$ gain: slope of the linear fit of the
885 firing frequency in the primary range; ΔF : difference between the instantaneous
886 firing frequency at de-recruitment and recruitment; V_{th} : voltage threshold for
887 spiking measured on the first spike of the ramp. **B.** Example of the response of a P35
888 mSOD1 mouse (same motoneuron as in Figure 1B). Same organization as in A. **C.**
889 Plot of the current intensity required for eliciting the first spike on a triangular ramp
890 of current in WT (blue squares) and mSOD1 motoneurons (red diamonds). WT:
891 slope= 0.1 nA/week 95%CI $[-0.11-0.31]$, $r^2=0.019$ ($p=0.34$). SOD1:
892 slope= -0.35 nA/week 95%CI $[-0.56--0.14]$, $r^2=0.2$ ($p=0.0019$). **D.** Breakdown of the
893 difference in recruitment current between WT and mSOD1 motoneurons in each of
894 the age groups. In young adult and presymptomatic mice, mutant motoneurons
895 require the same amount of current than WT motoneuron to fire, P30–60 WT:
896 4.73 ± 3.14 nA, N=19 vs. mSOD1: 6.21 ± 2.51 nA, N=14; $g=0.50$ 95%CI $[-0.24-1.24]$;
897 $t(31)=-1.51$, $p=0.14$. P60–90 WT: 5.28 ± 2.64 nA, N=16 vs. mSOD1: 4.53 ± 3.38 nA,

898 $N=20$; $g=-0.24$ 95%CI $[-0.93-0.41]$; $t(34)=0.75$, $p=0.46$. At the symptomatic stages
 899 (P90–120), mutant motoneurons exhibit a lower current threshold for firing (WT:
 900 5.43 ± 3.07 nA, $N=15$ vs. mSOD1: 2.19 ± 1.56 nA, $N=13$; $g=-1.26$ 95%CI $[-1.95--0.47]$;
 901 $t(26)=3.59$, $p=0.0017$), compatible with the loss of the least excitable cells. **E.** The
 902 slope of the F-I relationship, measured over the primary range, is not affected by the
 903 mutation, regardless of the age of the animals. WT: slope $=-0.13$ Hz/nA/week
 904 95%CI $[-0.65-0.38]$, $r^2=0.011$ ($p=0.6$). SOD1: slope $=0.27$ Hz/nA/week 95%CI $[-0.23-$
 905 $0.77]$, $r^2=0.028$ ($p=0.28$). **F.** Breakdown of the difference between WT and mSOD1
 906 motoneurons by age group: P30–60 WT: 9.3 ± 3.6 Hz/nA, $N=10$ vs. mSOD1:
 907 8.3 ± 3.4 Hz/nA, $N=14$; $g=-0.28$ 95%CI $[-1.10-0.64]$; $t(22)=0.69$, $p=0.5$. P60–90 WT:
 908 12.2 ± 7.3 Hz/nA, $N=8$ vs. mSOD1: 10.3 ± 6.4 Hz/nA, $N=16$; $g=-0.27$ 95%CI $[-1.22-$
 909 $0.54]$; $t(22)=0.62$, $p=0.54$. P90–120 WT: 8.0 ± 3.2 Hz/nA, $N=10$ vs. mSOD1:
 910 10.8 ± 9.1 Hz/nA, $N=13$; $g=0.38$ 95%CI $[-0.43-0.93]$; $t(21)=-1.04$, $p=0.31$.

911 **Figure 3: Young mutant motoneurons have an aberrantly large input**
 912 **conductance**

913 **A.** Plot of the motoneuron input conductance vs. age in WT (blue squares) and
 914 mSOD1 (red diamonds) animals. The solid lines correspond to the linear regression
 915 lines with 95% confidence intervals (shaded areas). WT slope $=0.018$ μ S/week
 916 95%CI $[0.0061-0.029]$, $r^2=0.16$ ($p=0.0035$); SOD1 slope $=-0.041$ μ S/week
 917 95%CI $[-0.052--0.03]$, $r^2=0.53$ ($p=6.1e-10$.) **B.** Breakdown of the difference in
 918 input conductance between WT and mSOD1 animals by age groups. P30–60 WT:
 919 0.42 ± 0.16 μ S, $N=19$ vs. mSOD1: 0.72 ± 0.18 μ S, $N=15$; $g=1.73$ 95%CI $[0.92-2.41]$;
 920 $t(32)=-5.06$, $p=2.2e-05$. P60–90 WT: 0.46 ± 0.16 μ S, $N=16$ vs. mSOD1: 0.42 ± 0.15 μ S,

921 N=24; $g=-0.28$ 95%CI[-0.96-0.37]; $t(38)=0.88$, $p=0.39$. P90-120 WT: 0.60 ± 0.15 μ S,
 922 N=15 vs. mSOD1: 0.33 ± 0.13 μ S, N=14; $g=-1.85$ 95%CI[-2.57--1.16]; $t(27)=5.16$,
 923 $p=2.1e-05$.

924 **Figure 4. The resting membrane potential of young adult mutant mice is**
 925 **hyperpolarized**

926 **A.** Plot of the motoneuron resting membrane potential vs. age in WT (blue
 927 squares) and mSOD1 (red diamonds) animals. The solid lines correspond to the
 928 linear regression lines with 95% confidence intervals (shaded areas). WT:
 929 slope= -0.068 mV/week 95%CI[-0.52-0.38], $r^2=0.0019$ ($p=0.76$). SOD1:
 930 slope= 0.81 mV/week 95%CI[0.31-1.3], $r^2=0.18$ ($p=0.0022$). **B.** Breakdown of the
 931 difference in resting membrane potential between WT and mSOD1 animals by age
 932 groups. P30-60 WT: -62.38 ± 5.52 mV, N=19 vs. mSOD1: -71.45 ± 8.78 mV, N=15;
 933 $g=-1.24$ 95%CI[-2.13--0.23]; $t(32)=3.49$, $p=0.002$. P60-90 WT: -60.98 ± 5.35 mV,
 934 N=16 vs. mSOD1: -66.18 ± 5.63 mV, N=22; $g=-0.92$ 95%CI[-1.54--0.18]; $t(36)=2.89$,
 935 $p=0.0067$. P90-120 WT: -64.71 ± 7.42 mV, N=15 vs. mSOD1: -61.99 ± 5.43 mV, N=13;
 936 $g=0.40$ 95%CI[-0.35-1.10]; $t(26)=-1.12$, $p=0.27$.

937 **Figure 5. Some motoneurons exhibit properties outside of the normal range**

938 **A.** Plot of the PIC amplitude vs. the input conductance of young adult
 939 motoneurons (P30-60) in WT (blue squares) and mSOD1 (red diamonds) animals.
 940 The grey line is the best linear fit \pm 95% confidence interval (shaded area) for both
 941 samples. Slope= 7.7 mV 95%CI[2.6-12.7], $r^2=0.55$ ($p=0.004$). The marginal plots
 942 indicate the kernel density estimation of the distributions of the values in the two
 943 populations. The ‡ symbol points to the fraction of the mSOD1 population that is

944 outside the range of the WT population. **B.** Same as A for the presymptomatic age
945 range P60–90. Slope=5.4 mV 95%CI[1.1–9.8], $r^2=0.15$ ($p=0.016$). **C.** Same as A for
946 the symptomatic age range P90–120. Slope=7.0 mV 95%CI[–0.8–14.9], $r^2=0.23$
947 ($p=0.078$).

948 **Figure 6: Some cells are hypoexcitable and cannot fire repetitively**

949 **A.** Example of an mSOD1 motoneuron (from a P88 mouse) that is unable to fire
950 repetitively in response to a triangular ramp of current. Top trace: membrane
951 potential, bottom trace: injected current. **B.** This same motoneuron was
952 nevertheless able to generate a single full-height action potential in response to a
953 square pulse of current. Same organization as in A. **C.** Voltage-clamp measurement
954 of the PICs in this same motoneuron. Traces are (from top to bottom), leak current
955 (dashed line), raw current (blue), leak-subtracted current (red) and voltage
956 command (green). **D.** Non-firing motoneurons had a similar input conductance
957 compared to motoneurons capable of firing repetitively. Firing: $0.49 \pm 0.22 \mu\text{S}$, $N=47$
958 vs. non-firing: $0.38 \pm 0.20 \mu\text{S}$, $N=6$; $g=-0.54$ 95%CI[–1.11–0.50]; $t(51)=1.36$, $p=0.22$ **E.**
959 Non-firing motoneurons had much smaller PICs than motoneurons able to fire
960 repetitively. Firing: $4.04 \pm 3.18 \text{ nA}$, $N=47$ vs. non-firing: $0.60 \pm 0.49 \text{ nA}$, $N=6$;
961 $g=-1.12$ 95%CI[–1.42––0.86]; $t(51)=6.81$, $p=1.3e-08$ **F.** Non-firing motoneurons
962 appear earlier in mSOD1 animals compared to WT animals. WT: 100 ± 16 days old,
963 $N=7$ vs. SOD1: 75 ± 23 days old, $N=6$; $g=-1.20$ 95%CI[–2.06–0.01]; $t(11)=2.24$,
964 $p=0.053$.

965 **Figure 7. Overview of the change in principal components over time.**

966 **A₁₋₃**. Plot of the three first principal components vs. age in WT (blue squares) and
967 mSOD1 motoneurons (red diamonds). The solid lines correspond to the linear
968 regression lines with 95% confidence intervals (shaded areas). **B**. Heatmap showing
969 the correlation coefficient between each principal component (columns) and the
970 features (rows) shown on the right. Correlation coefficients are color-coded from
971 dark blue ($r=-1$) to dark red ($r=+1$). **C**. Summary of the evolution of the difference
972 between WT and mSOD1 motoneurons (quantified by the effect size Hedges' g) for
973 each of the features and each of the time points considered. The features are
974 ordered by the size of the effect of the mutation in the P30–60 age group. On each
975 row, the dashed line represents an effect size of zero. Scale bar: 2 units.

976 **Figure 8: summary of the changes in motoneuron properties over time**

977 Schematic representation of the changes in four key electrophysiological
978 properties over time. The dots represent the effect size (Hedges' g) and the vertical
979 bars show the 95%CI around g . The thin lines are cubic splines interpolation of the
980 data over time. The points have been slightly staggered so that the vertical bars do
981 not occlude each other. †Data from embryonic motoneurons are from Martin et al.
982 (2013). These authors did not measure PICs in embryonic motoneurons. Kuo et al.
983 (2004) did measure PICs, but their embryonic motoneurons were cultured for 10–
984 30 days in vitro, and their development stage is therefore uncertain. ‡Data from
985 neonates (P0–5 and P6–12) are from Quinlan et al. (2011).

986 **Table 1: summary of the properties of the motoneurons, broken down by age**
987 **range**

988 The table shows the various properties that were measured in each motoneuron.

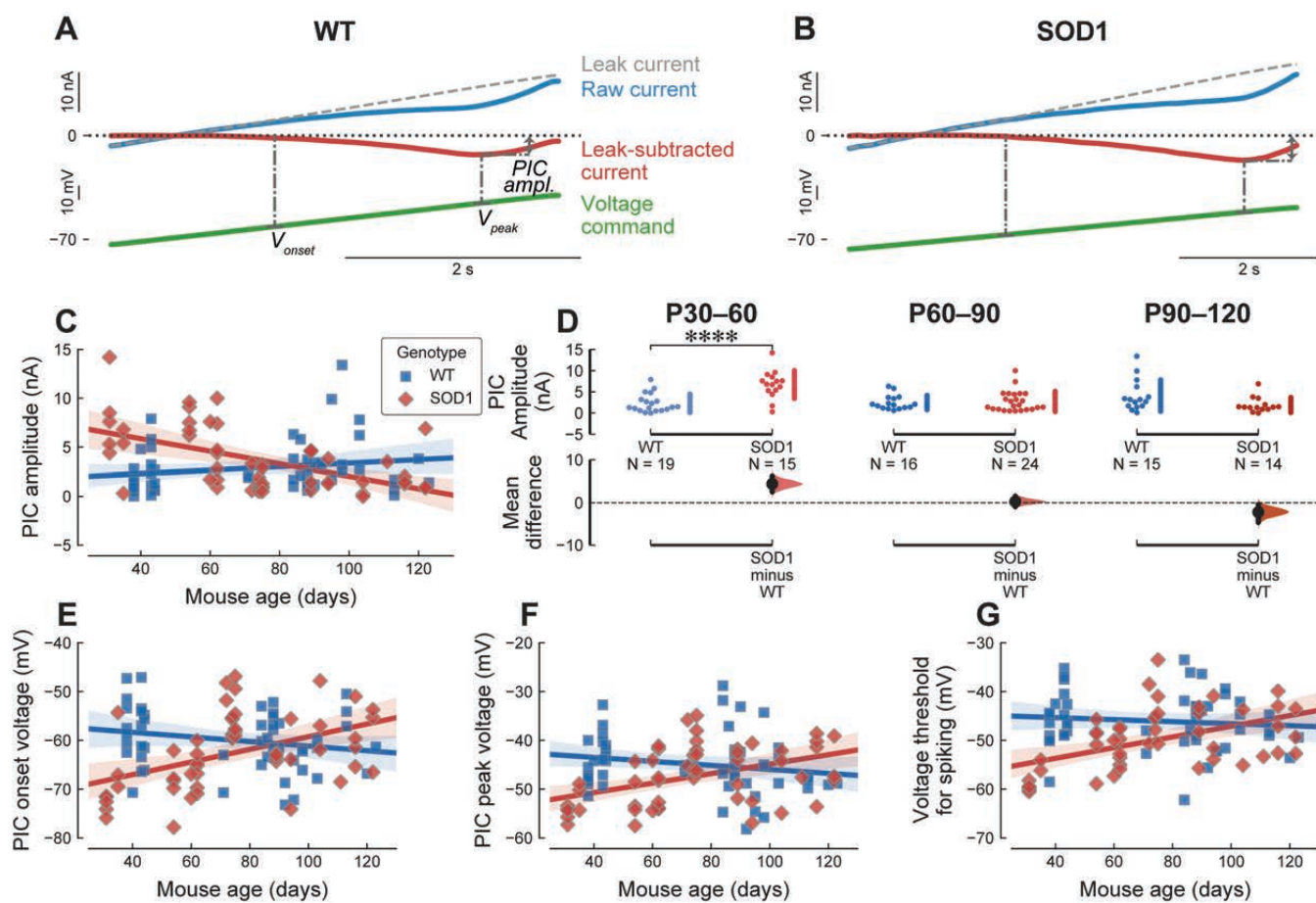
989 The rows are sorted in descending order of effect size at P30–60. WT and mSOD1

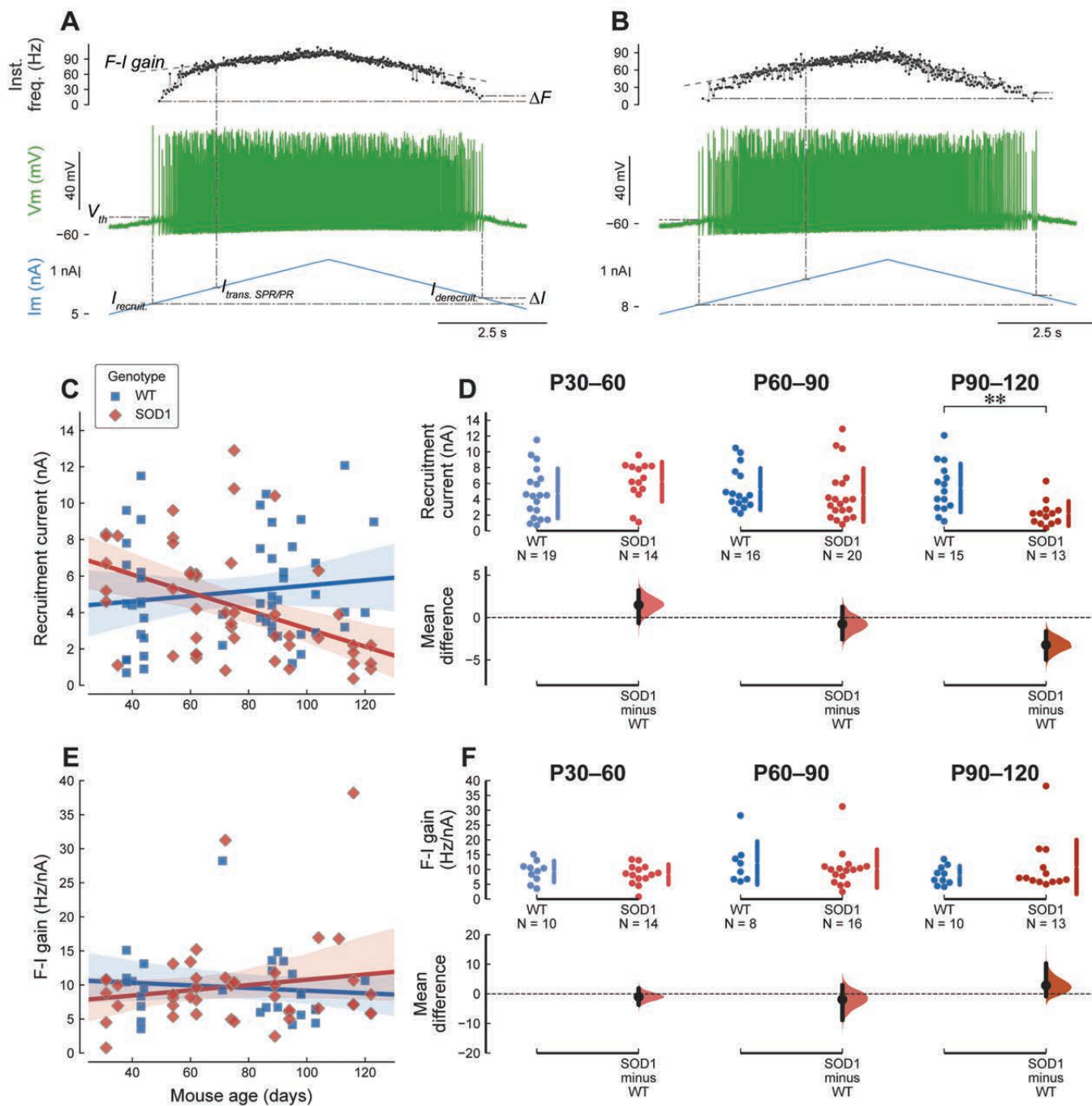
990 columns show mean values \pm standard deviation, with the 95%CI around the mean

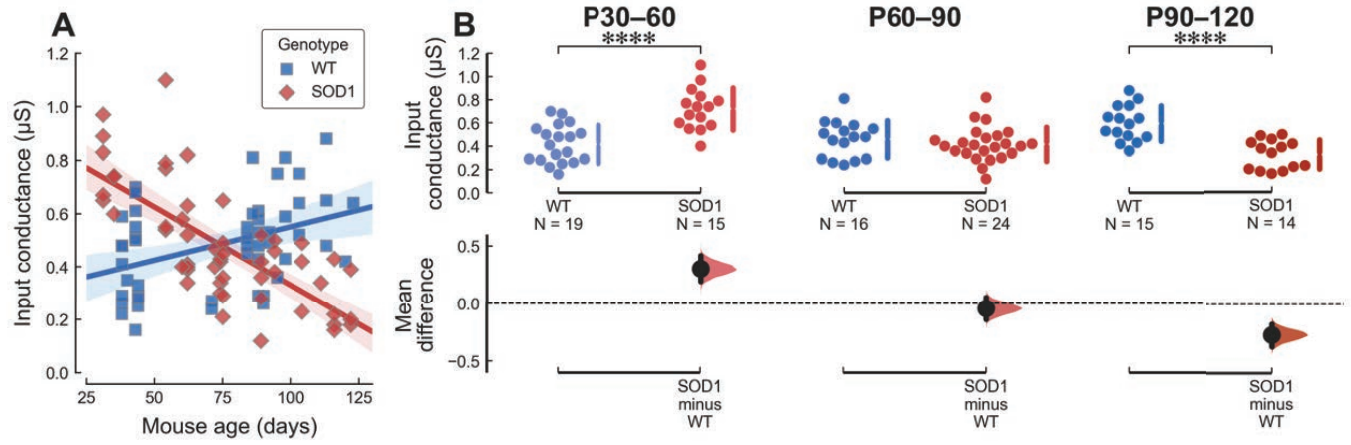
991 below. The "Mean diff." column shows the mean difference between mSOD1 and WT

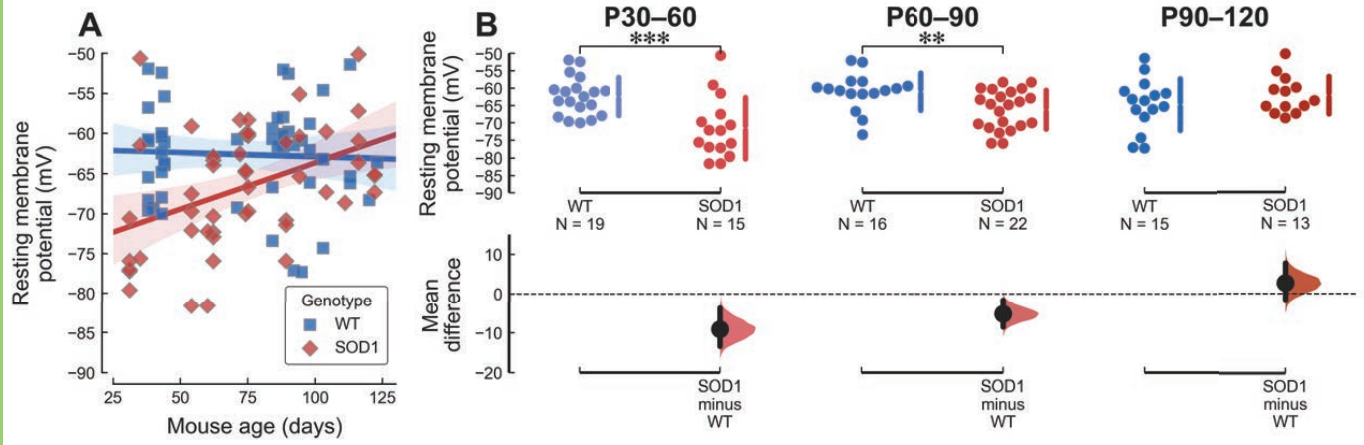
992 population, with 95% CI and the result of Welch's test (for information). The

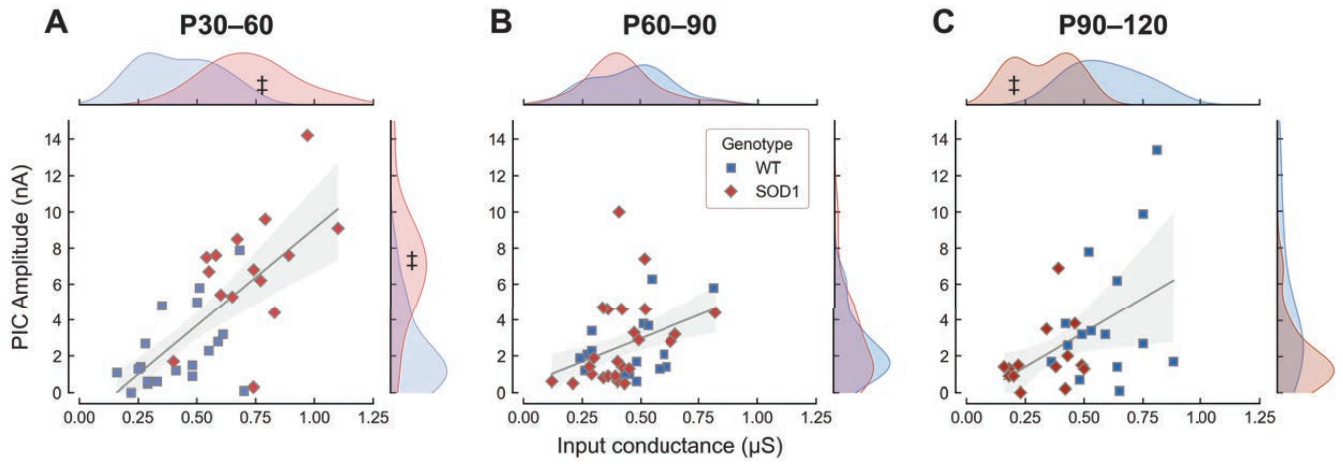
993 "Hedges' g " column shows the effect size and its 95%CI below.

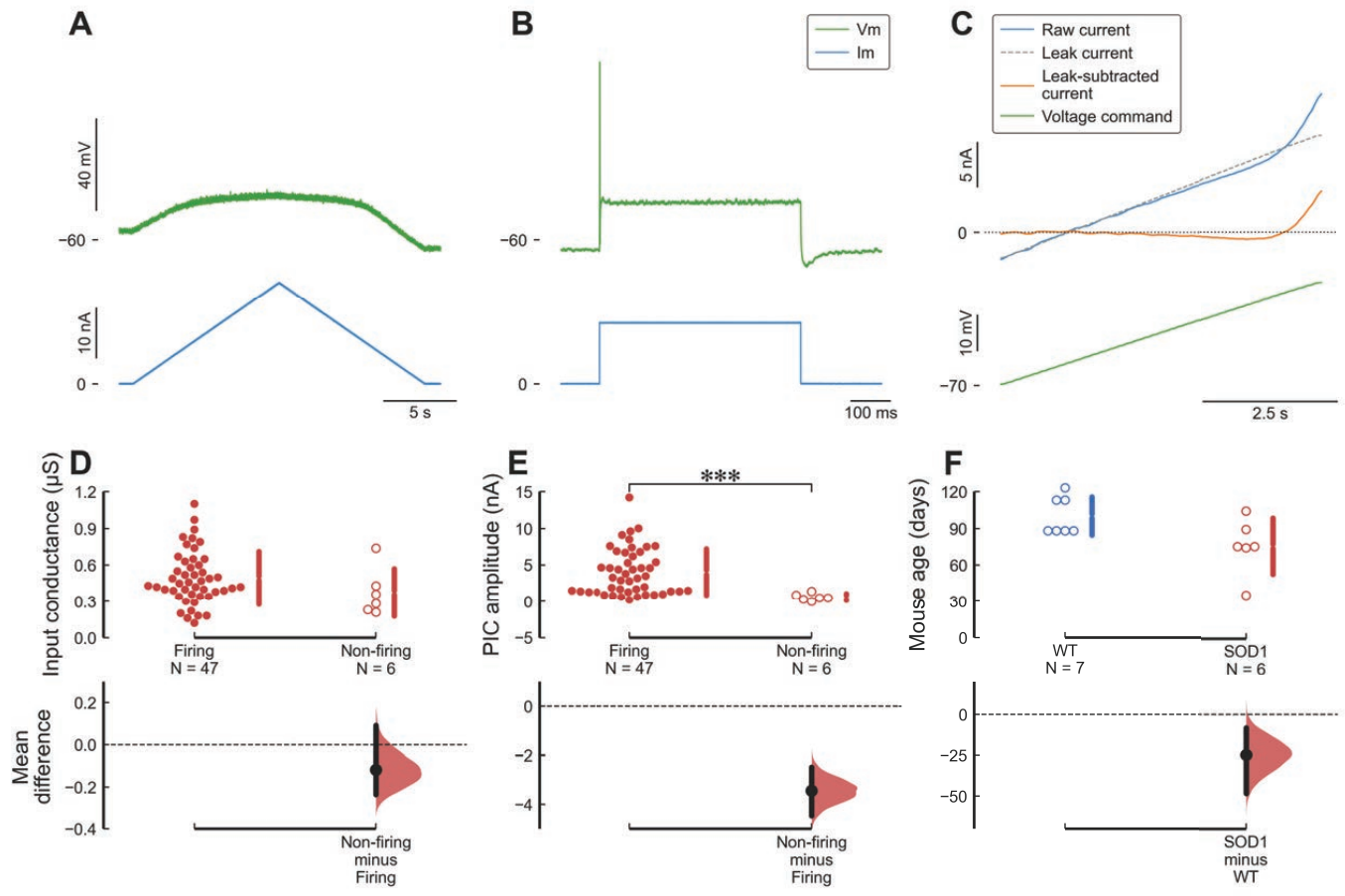


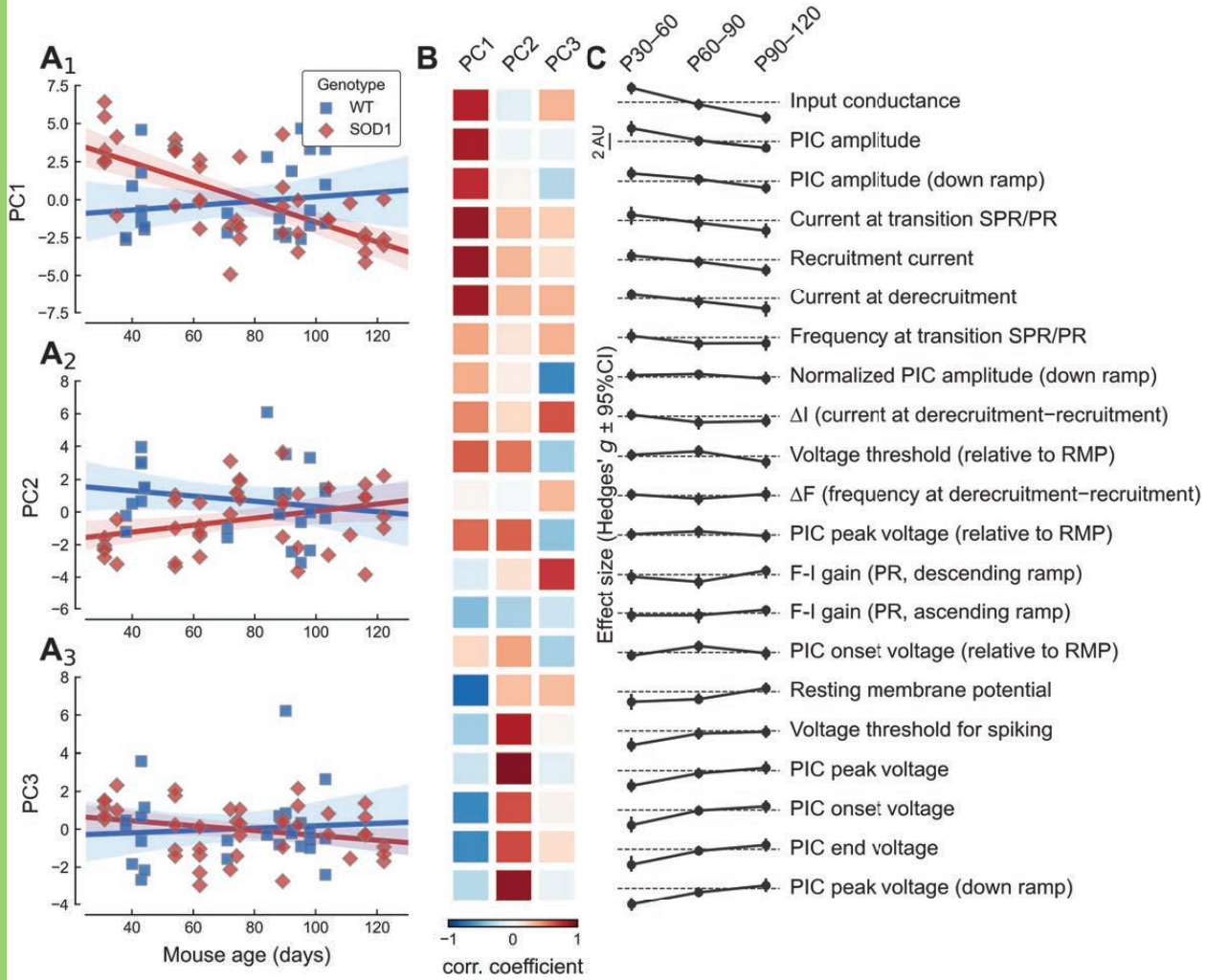


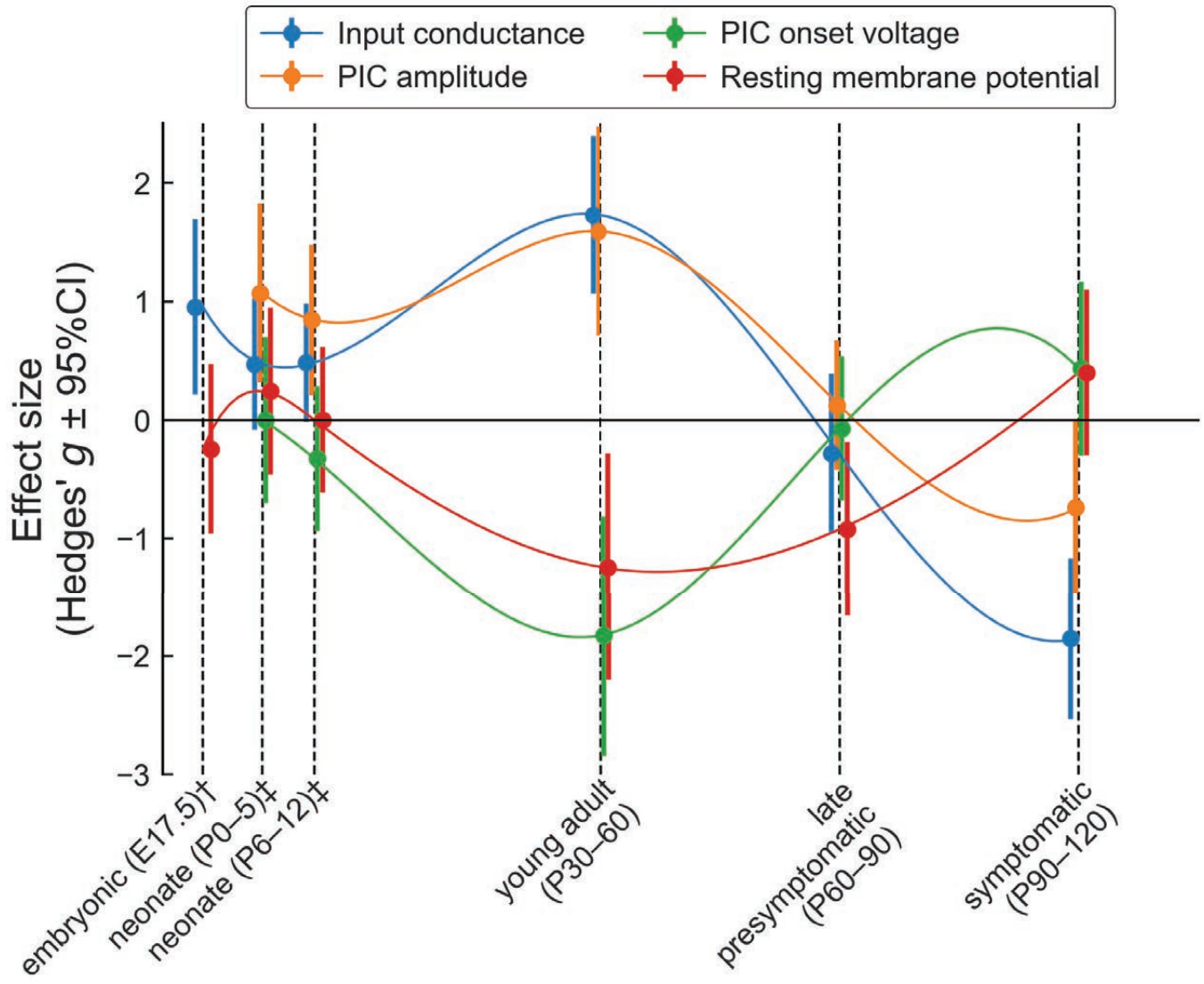












	P30-60				P60-90				P90-120			
	WT (N=19)	SOD1 (N=15)	Mean diff.	Hedges' g	WT (N=16)	SOD1 (N=24)	Mean diff.	Hedges' g	WT (N=15)	SOD1 (N=14)	Mean diff.	Hedges' g
Input conductance	0.42±0.16 μS [0.35-0.49]	0.72±0.18 μS [0.64-0.82]	0.30 μS [0.19-0.42] (p=2.2e-05 ****)	1.73 [0.93-2.40]	0.46±0.16 μS [0.39-0.54]	0.42±0.15 μS [0.36-0.48]	-0.04 μS [-0.14-0.05] (p=0.39)	-0.28 [-0.96-0.39]	0.60±0.15 μS [0.53-0.67]	0.33±0.13 μS [0.26-0.39]	-0.27 μS [-0.37-0.17] (p=2.1e-05 ****)	-1.85 [-2.57-1.17]
PIC amplitude	2.30±2.17 nA [1.52-3.45]	6.73±3.28 nA [5.18-8.51]	4.43 nA [2.56-6.29] (p=0.00016 ****)	1.59 [0.62-2.48]	2.47±1.69 nA [1.81-3.51]	2.75±2.40 nA [1.97-3.89]	0.27 nA [-0.93-1.53] (p=0.67)	0.12 [-0.53-0.67]	4.12±3.69 nA [2.67-6.40]	1.90±1.78 nA [1.24-3.19]	-2.22 nA [-4.63-0.41] (p=0.05)	-0.74 [-1.27-0.00]
PIC amplitude (down ramp)	2.65±2.60 nA [1.76-4.16]	5.55±3.48 nA [4.01-7.45]	2.90 nA [0.96-4.89] (p=0.013 *)	0.94 [0.15-1.70]	2.29±2.30 nA [1.52-4.01]	2.87±2.22 nA [2.12-3.87]	0.58 nA [-1.03-1.76] (p=0.44)	0.25 [-0.50-0.82]	4.43±3.10 nA [3.03-6.09]	2.25±1.98 nA [1.48-3.56]	-2.18 nA [-3.99-0.34] (p=0.032 *)	-0.81 [-1.49-0.03]
Current at transition SPR/PR	5.93±3.24 nA [4.37-8.51]	8.01±2.67 nA [6.54-9.24]	2.08 nA [-0.95-4.08] (p=0.13)	0.69 [-0.48-1.68]	6.28±3.92 nA [4.32-9.67]	5.23±3.30 nA [3.99-7.23]	-1.04 nA [-4.72-1.39] (p=0.53)	-0.29 [-1.34-0.48]	5.90±2.70 nA [4.24-7.38]	2.70±2.34 nA [1.18-3.76]	-3.20 nA [-5.24-1.28] (p=0.0081 **)	-1.23 [-2.07-0.35]
Recruitment current	4.73±3.14 nA [3.50-6.23]	6.21±2.51 nA [4.77-7.27]	1.49 nA [-0.65-3.22] (p=0.14)	0.50 [-0.25-1.26]	5.28±2.64 nA [4.19-6.79]	4.53±3.38 nA [3.35-6.35]	-0.76 nA [-2.57-1.27] (p=0.46)	-0.24 [-0.94-0.43]	5.43±3.07 nA [4.07-7.16]	2.19±1.56 nA [1.59-3.32]	-3.24 nA [-4.98-1.63] (p=0.0017 **)	-1.26 [-1.96-0.52]
Current at derecruitment	5.92±3.76 nA [4.38-7.65]	7.64±3.31 nA [5.91-9.24]	1.72 nA [-0.73-3.94] (p=0.17)	0.47 [-0.24-1.19]	6.54±4.07 nA [4.69-9.12]	5.01±4.05 nA [3.54-7.04]	-1.53 nA [-4.41-1.18] (p=0.31)	-0.37 [-1.16-0.33]	5.64±2.95 nA [4.03-7.22]	2.59±1.58 nA [1.93-3.64]	-3.05 nA [-4.75-1.24] (p=0.0056 **)	-1.26 [-2.23-0.37]
Frequency at transition SPR/PR	54.30±17.35 Hz [45.49-66.17]	57.90±17.06 Hz [49.74-66.74]	3.60 Hz [-10.88-15.87] (p=0.62)	0.20 [-0.65-1.04]	53.55±13.32 Hz [44.57-62.21]	43.75±13.55 Hz [36.99-49.60]	-9.79 Hz [-20.63-0.31] (p=0.11)	-0.70 [-1.52-0.09]	51.58±15.41 Hz [41.70-59.94]	42.44±11.34 Hz [36.74-48.89]	-9.14 Hz [-19.10-1.70] (p=0.13)	-0.67 [-1.58-0.23]
Normalized PIC amplitude (down ramp)	6.72±5.77 nA/μS [4.50-9.57]	7.85±4.85 nA/μS [5.49-10.58]	1.13 nA/μS [-2.42-4.63] (p=0.56)	0.20 [-0.48-0.96]	5.05±4.43 nA/μS [3.38-7.73]	6.81±5.14 nA/μS [5.24-9.34]	1.75 nA/μS [-4.16-4.57] (p=0.26)	0.35 [-0.35-0.89]	7.77±5.24 nA/μS [5.46-10.56]	6.72±4.91 nA/μS [4.77-9.82]	-1.05 nA/μS [-4.38-2.82] (p=0.58)	-0.20 [-0.92-0.60]
ΔI (current at derecruitment- recruitment)	1.20±1.20 nA [0.69-1.74]	1.45±1.25 nA [0.89-2.17]	0.25 nA [-0.54-1.10] (p=0.57)	0.20 [-0.49-0.87]	1.47±1.83 nA [0.57-2.52]	0.42±1.10 nA [-0.01-0.94]	-1.04 nA [-2.22-0.05] (p=0.093)	-0.72 [-1.57-0.05]	0.98±1.32 nA [0.38-1.78]	0.39±0.63 nA [0.05-0.71]	-0.53 nA [-1.50-0.13] (p=0.18)	-0.55 [-1.28-0.27]
Voltage threshold (relative to RMP)	17.03±6.37 mV [14.16-19.76]	18.09±5.21 mV [15.10-20.44]	1.05 mV [-3.07-4.74] (p=0.61)	0.17 [-0.53-0.86]	15.59±5.54 mV [13.26-18.55]	19.26±6.29 mV [16.80-22.24]	3.67 mV [-0.33-7.32] (p=0.072)	0.60 [-0.13-1.26]	17.10±5.54 mV [14.32-19.66]	13.79±3.62 mV [12.09-15.77]	-3.31 mV [-6.66-0.11] (p=0.071)	-0.67 [-1.44-0.15]
ΔF (frequency at derecruitment- recruitment)	1.79±13.96 Hz [-5.29-7.01]	3.77±11.06 Hz [-1.51-9.55]	1.98 Hz [-5.93-10.90] (p=0.65)	0.15 [-0.56-0.80]	6.53±17.29 Hz [0.25-21.46]	1.93±8.73 Hz [-1.51-6.16]	-4.60 Hz [-19.62-2.62] (p=0.4)	-0.36 [-1.12-0.37]	-0.85±7.97 Hz [-4.64-4.12]	0.75±7.97 Hz [-3.66-4.64]	1.60 Hz [-5.07-7.19] (p=0.62)	0.19 [-0.66-1.04]
PIC peak voltage (relative to RMP)	18.32±7.08 mV [15.26-21.42]	19.13±8.15 mV [14.28-22.51]	0.81 mV [-4.99-5.20] (p=0.76)	0.10 [-0.61-0.82]	18.09±7.71 mV [15.11-22.59]	21.18±5.82 mV [19.14-23.99]	3.09 mV [-1.76-6.94] (p=0.19)	0.45 [-0.34-1.10]	16.37±8.32 mV [12.41-20.31]	15.60±5.86 mV [12.55-18.63]	-0.77 mV [-6.08-4.36] (p=0.78)	-0.10 [-0.87-0.66]
F-I gain (PR, descending ramp)	19.21±10.07 Hz/nA [15.19-29.17]	17.23±5.15 Hz/nA [14.91-20.03]	-1.98 Hz/nA [-12.04-2.61] (p=0.58)	-0.25 [-1.15-0.58]	33.93±35.75 Hz/nA [18.24-75.19]	15.25±8.95 Hz/nA [11.99-21.30]	-18.68 Hz/nA [-59.63-2.66] (p=0.22)	-0.88 [-1.69-0.11]	15.15±7.14 Hz/nA [11.73-20.87]	20.05±11.30 Hz/nA [15.50-28.05]	4.90 Hz/nA [-2.37-12.22] (p=0.23)	0.48 [-0.48-1.07]
F-I gain (PR, ascending ramp)	9.30±3.58 Hz/nA [7.08-11.31]	8.30±3.37 Hz/nA [6.42-9.86]	-1.00 Hz/nA [-3.68-1.83] (p=0.5)	-0.28 [-1.09-0.63]	12.18±7.30 Hz/nA [8.81-19.47]	10.28±6.43 Hz/nA [8.15-15.26]	-1.90 Hz/nA [-8.81-2.94] (p=0.54)	-0.27 [-1.23-0.53]	8.01±3.16 Hz/nA [6.33-10.08]	10.84±9.13 Hz/nA [7.69-19.20]	2.84 Hz/nA [-0.81-10.27] (p=0.31)	0.38 [-0.41-0.94]
PIC onset voltage (relative to RMP)	4.36±5.66 mV [1.69-6.68]	2.05±5.38 mV [-1.02-4.23]	-2.31 mV [-6.23-1.00] (p=0.23)	-0.41 [-1.05-0.28]	1.76±5.75 mV [-0.85-4.65]	6.12±5.54 mV [3.80-8.38]	4.36 mV [0.56-7.69] (p=0.025 *)	0.76 [0.01-1.40]	1.57±5.10 mV [-0.86-4.11]	0.92±5.94 mV [-1.76-4.48]	-0.64 mV [-4.57-3.45] (p=0.76)	-0.11 [-0.93-0.64]
Resting membrane potential	-62.38±5.52 mV [-64.71--59.91]	-71.45±8.78 mV [-75.13--66.37]	-9.07 mV [-13.37--3.66] (p=0.002 **)	-1.24 [-2.19--0.28]	-60.98±5.35 mV [-63.81--58.71]	-66.18±5.63 mV [-68.56--63.88]	-5.20 mV [-8.47--1.59] (p=0.0067 **)	-0.92 [-1.54--0.19]	-64.71±7.42 mV [-68.81--61.39]	-61.99±5.43 mV [-64.41--58.61]	2.72 mV [-1.57-7.73] (p=0.27)	0.40 [-0.32-1.10]

Voltage threshold for spiking	-45.35±5.48 mV [-47.79--43.03]	-54.86±5.15 mV [-57.21--52.17]	-9.51 mV [-12.79--5.75] (p=1.9e-05 ****)	-1.74 [-2.53--0.84]	-45.39±7.04 mV [-49.10--42.26]	-47.53±5.85 mV [-49.76--44.73]	-2.14 mV [-6.20--2.13] (p=0.34)	-0.33 [-1.04--0.38]	-47.61±5.00 mV [-49.94--45.17]	-48.20±5.41 mV [-50.94--45.31]	-0.59 mV [-4.24--2.98] (p=0.77)	-0.11 [-0.85--0.63]
PIC peak voltage	-43.83±4.79 mV [-45.74--41.49]	-52.32±4.20 mV [-54.10--50.00]	-8.49 mV [-11.41--5.52] (p=4.8e-06 ****)	-1.83 [-2.60--1.03]	-42.89±6.94 mV [-45.81--39.26]	-44.88±5.24 mV [-46.93--42.88]	-1.98 mV [-6.20--1.50] (p=0.34)	-0.33 [-0.97--0.33]	-48.34±5.89 mV [-50.89--45.11]	-46.24±6.27 mV [-49.56--43.26]	2.10 mV [-2.40--6.21] (p=0.36)	0.34 [-0.43--1.15]
PIC onset voltage	-58.03±6.35 mV [-60.91--55.34]	-69.41±5.71 mV [-71.66--66.01]	-11.38 mV [-14.95--7.18] (p=5.1e-06 ****)	-1.83 [-2.69--0.81]	-59.22±4.88 mV [-61.96--57.18]	-59.66±6.39 mV [-61.98--56.91]	-0.43 mV [-3.71--3.21] (p=0.81)	-0.07 [-0.70--0.54]	-63.15±6.31 mV [-65.99--59.85]	-60.12±7.25 mV [-63.92--56.48]	3.03 mV [-1.95--7.63] (p=0.24)	0.43 [-0.35--1.17]
PIC end voltage	-58.67±6.87 mV [-61.68--55.65]	-71.37±6.36 mV [-73.99--67.60]	-12.69 mV [-16.68--8.02] (p=4.1e-06 ****)	-1.86 [-2.69--0.80]	-60.48±4.90 mV [-63.57--58.66]	-61.80±7.27 mV [-64.75--58.95]	-1.32 mV [-4.61--2.66] (p=0.5)	-0.20 [-0.77--0.42]	-65.00±5.70 mV [-67.79--62.19]	-61.30±8.12 mV [-65.34--57.16]	3.70 mV [-1.44--8.54] (p=0.17)	0.52 [-0.28--1.27]
PIC peak voltage (down ramp)	-43.73±4.89 mV [-45.62--41.28]	-53.63±4.90 mV [-55.76--50.95]	-9.90 mV [-13.10--6.60] (p=2.1e-06 ****)	-1.97 [-2.78--1.17]	-42.49±8.15 mV [-45.71--37.94]	-45.85±6.11 mV [-48.41--43.56]	-3.36 mV [-8.41--0.62] (p=0.17)	-0.47 [-1.08--0.16]	-48.14±5.25 mV [-50.45--45.05]	-45.98±6.26 mV [-49.54--43.13]	2.17 mV [-2.22--5.96] (p=0.32)	0.37 [-0.41--1.20]